Mathematical Biosciences 389 (2025) 109519

Contents lists available at ScienceDirect

Mathematical Biosciences

journal homepage: www.elsevier.com/locate/mbs

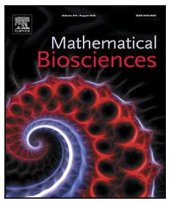

Original Research Article

A new optimized regularized Stokeslet model reveals the effects of multicellular protozoan colony configuration on hydrodynamic performance

Hongfei Chen [a,*], Tom Hata [b], Ricardo Cortez [a], Hoa Nguyen [c], M.A.R. Koehl [b,d], Lisa Fauci [a]

[a] Department of Mathematics, Tulane University, New Orleans, LA 70118, USA
[b] Department of Integrative Biology, University of California, Berkeley, CA 94720, USA
[c] Department of Mathematics, Trinity University, San Antonio, TX 78212, USA
[d] Santa Fe Institute, Santa Fe, NM 87501, USA

ARTICLE INFO

Keywords:
Choanoflagellates
Regularized Stokeslets
Multicellular microbial colonies
Viscous flow
Reduced hydrodynamic models

ABSTRACT

Many microbial eukaryotes have unicellular life stages, but can also form multicellular colonies. We explored hydrodynamic consequences of colony morphology, which affects swimming and flux of prey-carrying water to cells in a colony, using the choanoflagellate, *Choanoeca flexa*, which forms cup-like colonies that can turn inside-out so flagella line the cup's interior or cover its outside surface. Detailed hydrodynamic models incorporating cell morphologies are not feasible for colonies with many cells. Therefore, we designed a reduced model of each cell using regularized-force-dipoles with parameters optimized (by selecting the regularized delta function from a given class) to match the flow-field of a detailed model of a cell. Calculated swimming speeds and water flux to flagella-in colonies match those measured for living *C. flexa*. For a given shape (flat bowls, hemispheres, spherical cups) of flagella-in colony, models showed that swimming speed and water flux towards the colony increases with cell density, although flux per cell is independent of density. Denser packing of cells at the front of flagella-in colonies increases swimming speed and flux to cells at all positions in the colonies. Flagella-in colonies swim more slowly, but produce higher water flux per cell than do flagella-out colonies of the same configuration, suggesting that flagella-out colonies are better swimmers, whereas flagella-in colonies are better feeders. A model flagella-out colony with morphology matched to a real *C. flexa* requires a flagellar force 5–10 times greater than that for flagella-in colonies to achieve the measured swimming speed, suggesting flagella beat differently on flagella-out colonies.

1. Introduction

Microbial eukaryotes that eat bacteria are critical elements in aquatic food webs (e.g. [1,2]). Their swimming, feeding, and predator avoidance depend on their hydrodynamics. Although many microbial eukaryotes can form multicellular colonies, the consequences of colony morphology to their hydrodynamic performance are poorly understood. Here we focus on choanoflagellate protozoans to explore how aspects of colony design can affect their swimming and creation of feeding currents. Species of choanoflagellates that can be unicellular or form multicellular colonies of different designs by cell division [3], enable us to study within a single species the effects of colony formation and design on performance.

1.1. Choanoflagellates

Not only are choanoflagellates abundant in marine and freshwater habitats where they are important bacteria-consuming components food webs, but they are also of great interest evolutionarily (reviewed by [3,4]). The evolution of animals from protozoan ancestors had a profound effect on the history of life on Earth. Molecular phylogenetic and comparative genomic analyses have shown that choanoflagellates and animals shared a common ancestor (e.g. [5–7]). A choanoflagellate cell (Fig. 1(a)) swims by waving a single flagellum, which also creates a water current that carries bacterial prey to a collar of rod-like microvilli surrounding the flagellum. Sponges (primitive animals) have "flagellated chambers" lined by cells ("choanocytes") that have the same structure as choanoflagellates and that catch bacteria from the water they pump through the sponge [8,9]. Choanoflagellates are studied to provide insights about how the protozoan ancestors of animals might have functioned (e.g. [7,10–12]). By investigating aspects of the hydrodynamics of choanoflagellates that affect their ecological interactions, we can make informed inferences about possible selective

* Corresponding author.
E-mail address: hchen35@tulane.edu (H. Chen).

https://doi.org/10.1016/j.mbs.2025.109519
Received 9 April 2025; Received in revised form 4 August 2025; Accepted 8 August 2025
Available online 18 August 2025

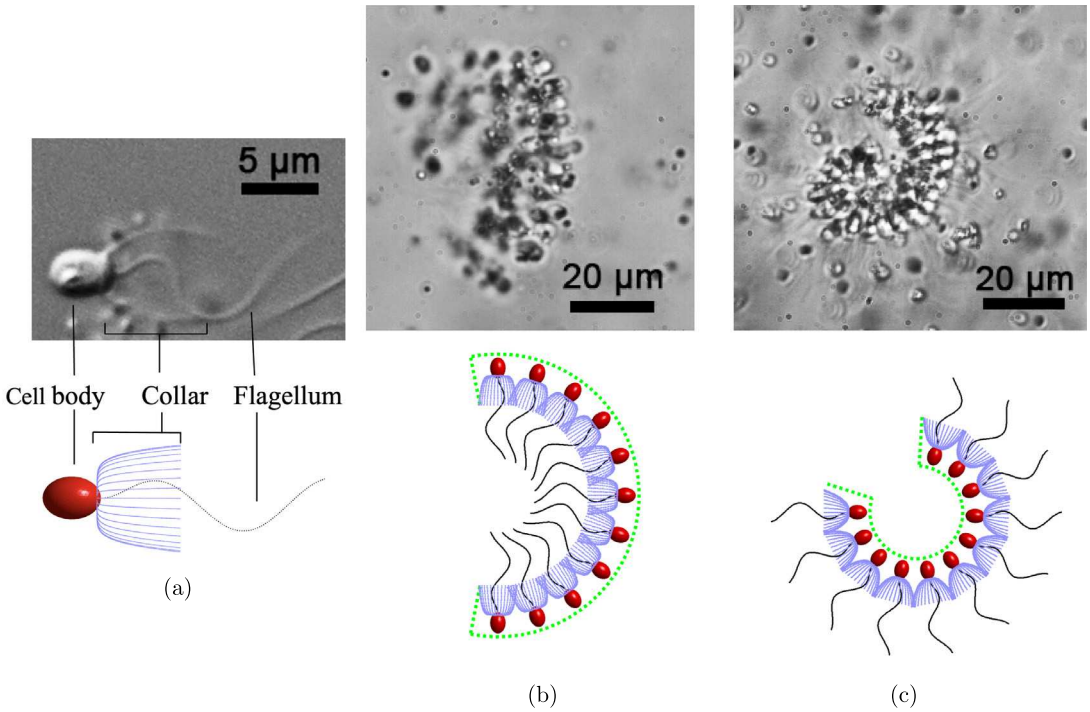

Fig. 1. Frames of videos of choanoflagellates and diagrams of cell and colony morphology. (a) A unicellular choanoflagellate has an ovoid cell body with a single flagellum surrounded by a collar of 20–40 microvilli. When the flagellum beats, the cell swims to the left and water is drawn past the collar, where bacterial prey are caught. (b) A flagella-in colony of *C. flexa* and a diagram of a cross-section of that colony. (c) A flagella-out colony of *C. flexa* and a diagram of a cross-section of that colony. The green dotted curves indicate the intake zones that will be used to calculate the flux of prey-carrying water to the colonies.

pressures on their ancestors at the time of animal origins (reviewed by [12]).

One critical step in the evolution of animals from a choanoflagellate-like ancestor was becoming multicellular. The choanoflagellates *Salpingoeca rosetta* and *Salpingoeca helianthica*, which have complex life cycles with unicellular and multicellular stages, have been used to study the molecular mechanisms involved with colony formation and sensation (reviewed by [7,13]) as well as the hydrodynamic and ecological consequences of being unicellular versus multicellular (reviewed by [12]). Experiments comparing the performance of unicellular versus multicellular stages of *S. rosetta* revealed that single cells are better swimmers, exploring the water for patches of prey bacteria [12,14], whereas cells in colonies feed at higher rates [12]. Although there is no difference between colonies and single cells of *S. helianthica* in the danger of being captured by passive protozoan predators [15], colonies put out larger hydrodynamic signals and are more susceptible to raptorial protozoan predators than are single cells [16], but are too large to be engulphed by suspension-feeding protozoan predators that can eat unicellular choanoflagellates [12].

S. rosetta and *S. helianthica* form colonies that are chains of cells or that are rosettes of cells with the flagella pointing outwards. An important morphological difference between choanoflagellate rosette colonies and sponges is that the flagella cover the outside surface of a rosette colony, whereas they point inwards, lining the walls of a cavity in a sponge flagellated chamber. We studied the choanoflagellate *Choancaeca flexa*, which forms cup-shaped colonies that can turn themselves inside-out in response to environmental signals such as changes in light or mechanical stimulation [11,13,17–21]. *C. flexa* enabled us to use just one species to compare the hydrodynamic consequences of having flagella covering a colony's outer surface versus lining a cavity, where the same cells could compose colonies of each configuration. Brunet at al. [11] observed that flagella-out colonies of *C. flexa* swam more rapidly than flagella-in colonies, whereas a greater proportion of the cells in flagella-in colonies ate microbeads than did the cells in flagella-out colonies. Therefore, they proposed that there is a trade-off between swimming and feeding performance of *C. flexa* colonies. By studying the hydrodynamics of each colony configuration, we can study the mechanisms responsible for these performance differences.

1.2. Modeling approaches for choanoflagellate hydrodynamics

Various simplifications have been made to model the hydrodynamics of choanoflagellates. Some species of choanoflagellates (including *S. rosetta*) have a unicellular life stage that is attached to a surface. Early approaches to modeling an attached unicellular choanoflagellate represented the flagellar dynamics by a line or helical arrangement of Stokeslets, and accounted for the collar of microvilli by prescribing a pressure drop that depended upon an assumed collar geometry (e.g. [22–24]). Smith [25] described a regularized Stokeslet method to simulate the flow produced by a flagellum. Nguyen et al. [26] used that approach and were the first to include the collar of microvilli into models of unicellular *S. rosetta* and to explore the complicated effects of the collar and flagellar dynamics on swimming and feeding performance. Similarly, Nielsen et al. [27] presented a detailed model representing the cell body, the microvilli, and the undulatory flagellum of the unicellular choanoflagellate *Diaphanoeca grandis*, which forms a basket-like structure ("lorica") that surrounds the cell and collar. They used the model to explore the effect of the lorica to the flow and forces on the flagella.

Building models of multicellular choanoflagellates using detailed models of each cell becomes computationally expensive as the number of cells in a colony increases, so a variety of simplifying approaches have been used. Roper et al. [28] measured the flow produced by a single attached *S. rosetta* and then represented each flagellum in their model by a point-force that generated a far-field flow matched to the measured one. They then constructed free-swimming colonies of different sizes and configurations, representing the flagellum of each cell by that point force. Kirkegaard & Goldstein [29] analyzed the flow produced by chain and rosette colonies of *S. rosetta*, modeling each cell with a rod-shaped flagellum and a spherical cell body, but no collar.

Recently, *C. flexa* colonies [30] have been modeled by cells distributed on spherical rafts driven by point-force flagella. Swimming speed and fluxes into the colony surface for various shapes were calculated, and colony inversion was modeled by actively changing curvatures of the colony geometry. Although these models do not incorporate the collars, they have enabled exploration of the effects of some aspects of colony design on the swimming and feeding performance of multicellular choanoflagellates.

In the study presented here, we designed a reduced model of a choanoflagellate cell using regularized-force-dipoles with parameters optimized to match the flow-field of a detailed model of a cell, and then used those force-dipoles to construct large cup-shaped flagella-in and flagella-out colonies. We tested this approach by comparing the performance of model colonies with that measured for *C. flexa* colonies. Then the models were used to explore the effects of various aspects of colony morphology on swimming speed and flux of prey-carrying water to the cells in a colony.

2. Methods

2.1. Measurements of living Choanoeca flexa

We used videomicrography to record the morphology, swimming, and water flow produced by flagella-in and flagella-out colonies of *C. flexa*, which were cultured as described by [11]. Because *C. flexa* stick to glass surfaces, we videotaped colonies in square plastic wells (15×15mm, height 0.8 mm) fabricated by gluing 3D-printed PLA walls to polycarbonate lids (35 mm diameter) of FluoroDishes (FD35-100, World Precision Instruments). Aliquots (220 μl) of *C. flexa* culture (taken 24 to 60 h after a culture had been passaged) were transferred into these wells using 3ml plastic transfer pipettes. Colonies in culture are flagella-in, so to videotape flagella-out colonies we induced colonies to turn inside-out by adding caffeine to produce a $10mM$ solution (details in [11]). We visualized water flow in these wells by tracking 1 μm polystyrene beads. We diluted 800 μl of a stock suspension of beads (Thermo Scientific 4009 A) in 10 ml of distilled water and added 12 μl of this diluted suspension to the culture in a well. We gently mixed the fluid in a well by slowly drawing then expelling the mixture three times using a 3 ml plastic pipette so that the beads were uniformly distributed. The well was then capped with a glass coverslip and was immediately viewed in bright field using a Leica DMLS microscope illuminated by a fiber-optic light source so that temperature in the well was kept at 20 °C. Using a magnification of 40x, videos were recorded at 30 fps using a HiSpec 1 camera (Fastec Imaging) for durations of 7–54 s. To minimize wall effects, all observations of swimming colonies were made at least 50 μm away from any surface. Videos were only made during the first 15 min after a well was prepared to avoid any artifacts that might be caused by the beads that the *C. flexa* captured on their collars. These videos were used to make morphological measurements of colonies using Image J or MATLAB software, to track particle paths and to determine swimming speeds using MTracker J software, and to measure water flow fields around colonies using Particle Image Velocimetry (PIV) software (DaVis 10.2, LaVision). All linear measurements were made to the nearest pixel and converted to μm (2.88 pixel/μm).

2.2. Mathematical model

2.2.1. Detailed model of choanoflagellates

At the small length scales of choanoflagellates, inertia does not play a part in their hydrodynamic performance, and, therefore, the flow around them is well-described by the incompressible Stokes equations. Nguyen et al. [26] presented a three-dimensional computational model of a single choanoflagellate in a Stokes fluid that explicitly represented the cell body, individual microvilli of the collar, and time-dependent flagellar dynamics. They demonstrated that morphological details did, indeed, affect swimming and feeding performance. Longer microvilli reduced speed and cell shape only affected speed when the collar of microvilli was very short. Using fluid flux through a capture zone as a proxy for bacterial prey capture, they found that models that ignore the collar overestimate flux and greatly overestimate the benefit of swimming to feeding performance.

Table 1
Geometric and waveform parameters used in the detailed computational model of a *C. flexa* cell.

Feature	Value	Reference
Cell length l_a	5 μm	c
Cell width l_b	3.7 μm	a
Microvilli length ℓ_{mi}	8 μm	a
Number of microvilli	32	b
Half angle of collar θ_{mi}	27.2°	a
Flagellum tapering parameter c	4 μm	a
Flagellum wave number k	$2\pi/16$ μm^{-1}	a
Flagellum amplitude A	2.5 μm	c
Flagellum beat frequency ω	30 Hz	c
Flagellum projected length L	19.2 μm	a
Flagellum arclength $\tilde{L}$	22.3 μm	a

a Model parameters for *C. flexa* measured or estimated from micrographs and TEMs in [11].
b Model parameters of *S. rosetta* from table 1 in [26].
c Measurements from Koehl lab posted at:
https://ib.berkeley.edu/labs/koehl/resint/multicellularity.html.

While the detailed model in [26] was based upon the solitary *S. rosetta*, here we have adjusted it to incorporate some measured features of *C. flexa* morphology (see Table 1). We make the assumption that the flagellum of the relaxed *C. flexa* cell undergoes a planar, sinusoidal motion during its beating and prescribe the kinematics as:

$$x(s,t) = s, \quad y(s,t) = A(1-\exp(-s/c))\sin(ks - 2\pi\omega t), \quad z(s,t) = 0, \quad 0 \le s \le L, \tag{1}$$

where s is arclength and $x(\cdot,t), y(\cdot,t), z(\cdot,t)$ is the curve describing the time-dependent shape of the planar flagellum. We also assume that the individual microvilli comprising the collar are rigid, and their shape is prescribed as

$$x(s,t) = s^5\,\ell_{\mathrm{mi}}\cos(\theta_{\mathrm{mi}}), \quad y(s,t) = s\,\ell_{\mathrm{mi}}\sin(\theta_{\mathrm{mi}}), \quad z(s,t) = 0, \quad 0 \le s \le 1. \tag{2}$$

Fig. 2 shows the computed streamlines and flow velocity magnitudes around three swimmers: one with no collar, one with a short collar, and one with a collar length typical for *C. flexa*. Here the streamlines are depicted in the flagellar plane above the centerline, and the velocities giving rise to these streamlines have been averaged over a flagellar beat period and over twelve half-planes at equally spaced angles around the x-axis. In each case, we see streamlines characteristic of *pushers*, where the flow along the axis of the swimmer points outwards, in opposite directions, at its front and back, and flow points inwards from above and below towards its middle. The vertical dashed red lines in each snapshot indicates the cell body centroid, and also the location of separatrix in the flow field away from the swimmer. We note that the location of this separatrix varies with collar length, and marches away from the cell body as the collar grows.

For a prescribed flagellar beat pattern, this detailed model identifies features of the fluid motion created by the organism in the immediate region around it and in the far field. When analyzing the flow features of a colony of choanoflagellates, which may contain dozens or hundreds of organisms, such a detailed model becomes computationally expensive as the number of colony members grows. To analyze the collective motion of many choanoflagellates, we choose to represent each member by a *reduced model* consisting of a single regularized element that approximates the time-averaged far-field flow generated by the detailed model, so that there is consistency in the far-field

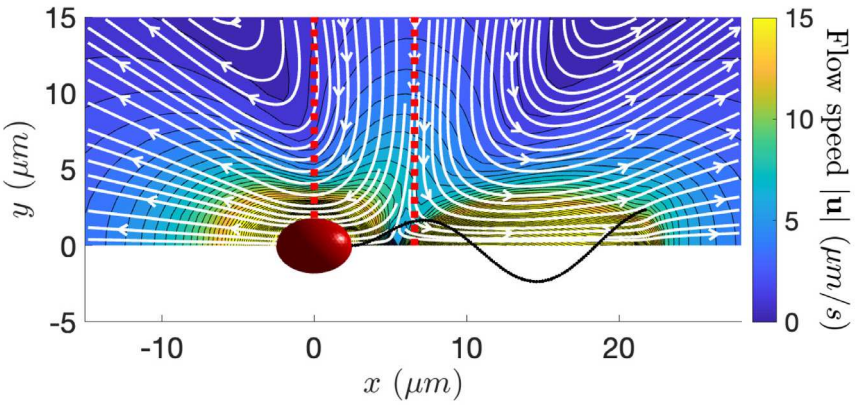

(a)

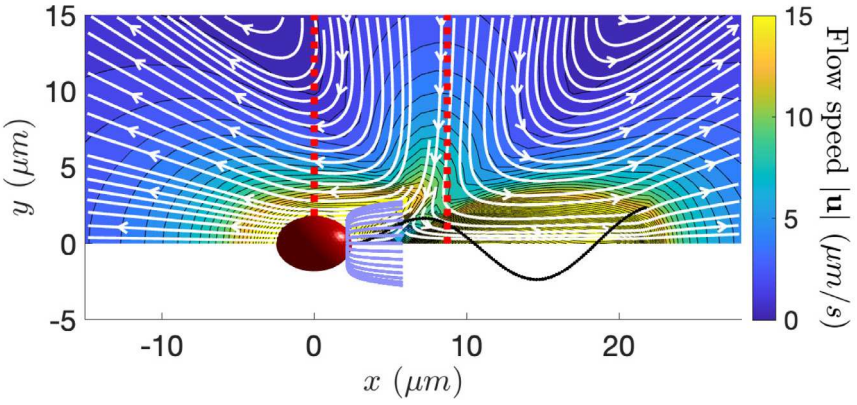

(b)

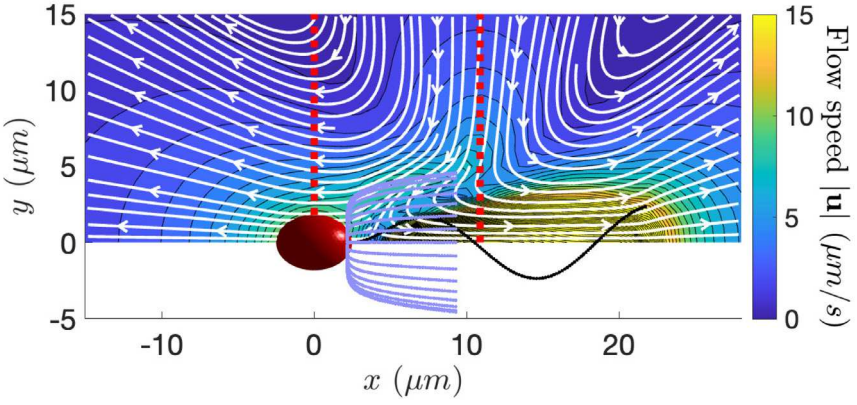

(c)

Fig. 2. Streamlines and flow velocity magnitudes above the flagellar axis averaged over one beat period and over twelve half-planes at equally spaced angles around the x-axis, for three swimmers: (a) no collar, (b) short collar, and (c) full collar. Dashed red lines indicate position of cell center and separatrix of the pusher flow field. Here the flow was computed using a detailed morphological model as in [26].

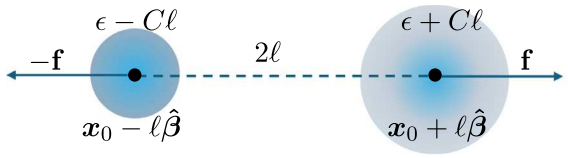

Fig. 3. Schematic of the configuration of two equal and opposite regularized Stokeslets prior to the limiting process that takes $\ell \to 0$. The regularization parameters $\epsilon - C\ell$ and $\epsilon + C\ell$ converge to the same value ϵ as $\ell \to 0$.

fluid velocity produced by the two models. This approach of using reduced models of single cells to study the fluid dynamics of colonies of choanoflagellates was used in [28] and more recently in [30,31].

2.2.2. Reduced model preliminaries

The basic situation of a flagellum pushing fluid backward while the cell body swims forward gives rise to a simple model of a self-propelled organism consisting of a force dipole (stresslet) [32,33], which decays as r^{-2} with the distance r from the organism. Other models related to the force-dipole model represent an organism by two or a few point singularities [30,34–36], as two spheres [37], or as a small sphere with prescribed surface velocity (squirmer) [38–40]. In [41,42], the force-dipole model was extended to include a potential dipole at the same location as the stresslet, which breaks the fore-aft symmetry to provide propulsion.

Here, we use this formulation [41,42] where the regularized elements are located at a single point. The placement of this point, relative to the virtual cell body center, will be selected as part of our optimization procedure so that the far-field flow produced by this reduced model approximates the fluid flow computed using the detailed morphological model. As part of this new approach, the regularizing function used in the regularized Stokeslet formulation is not preset, rather some parameters of this function are selected in our optimization procedure. This will be described in detail below.

In $\mathbb{R}^3$, the velocity induced by a single regularized force $\boldsymbol{f}$ applied at $\boldsymbol{x}_0$ is the regularized Stokeslet, which can be written in the form

$$\mathbf{u}(\boldsymbol{x}_e) = \boldsymbol{S}(\boldsymbol{x},\epsilon)\mathbf{f} = H_1(r,\epsilon)\mathbf{f} + (\mathbf{f}\cdot\boldsymbol{x})\boldsymbol{x}H_2(r,\epsilon) \tag{3}$$

where $\boldsymbol{x} = \boldsymbol{x}_e - \boldsymbol{x}_0$ and $r = |\boldsymbol{x}|$, and $\boldsymbol{x}_e$ is the evaluation point. This expression is the exact solution of the Stokes equations $\nabla\cdot\mathbf{u} = 0$, $\mu\Delta\mathbf{u} - \nabla p = -\mathbf{f}\phi_\epsilon(r)$. Here, $\mathbf{u}$ is the fluid velocity, p is the pressure, μ is the fluid viscosity, $\mathbf{f}$ is a force coefficient, and ϵ is a small positive length so that $\phi_\epsilon(r)$ is a smooth approximation of the Dirac delta function and is localized in a small sphere centered at the point $\boldsymbol{x}_0$, where the force is applied [43,44]. The regularization parameter ϵ is part of $H_1(r,\epsilon)$ and $H_2(r,\epsilon)$.

As depicted in Fig. 3, we adapt the model in [37] and place two equal but opposite forces at a distance 2ℓ from each other:

$$\boldsymbol{S}(\boldsymbol{x}_e - \boldsymbol{x}_0 - \ell\hat{\boldsymbol{\beta}};\epsilon + C\ell)\mathbf{f} - \boldsymbol{S}(\boldsymbol{x}_e - \boldsymbol{x}_0 + \ell\hat{\boldsymbol{\beta}};\epsilon - C\ell)\mathbf{f}.$$

For self-propulsion, it is important that the two forces be regularized with different parameters, which has been included in the expression above by using the regularization parameters $\epsilon + C\ell$ and $\epsilon - C\ell$. This breaks the aft-fore symmetry in the model and determines a swimming direction.

Setting $\mathbf{f} = (q_0/2\ell)\hat{\boldsymbol{\beta}}$ and taking the limit as $\ell \to 0$ while keeping q_0 fixed gives the force-dipole fluid velocity at evaluation point $\boldsymbol{x}_e$:

$$\mathbf{u}^{fd}(\boldsymbol{x}_e) = -q_0(\hat{\boldsymbol{\beta}}\cdot\nabla)\boldsymbol{S}(\boldsymbol{x},\epsilon)\hat{\boldsymbol{\beta}} + Cq_0\frac{\partial}{\partial\epsilon}\boldsymbol{S}(\boldsymbol{x},\epsilon)\hat{\boldsymbol{\beta}}, \text{ where } \boldsymbol{x} = \boldsymbol{x}_e - \boldsymbol{x}_0.$$

The last term is simplified by writing it in terms of derivatives with respect to $r = |\boldsymbol{x}|$ [41,42] and using the decay rates $H_1(r,\epsilon) \sim r^{-1}$ and $H_2(r,\epsilon) \sim r^{-3}$ for large r. These imply that $H_1(r,\epsilon) = \epsilon^{-1}H_1(r/\epsilon,1)$ and $H_2(r,\epsilon) = \epsilon^{-3}H_2(r/\epsilon,1)$, which can be combined into the single expression $H_k(r,\epsilon) = \epsilon^{1-2k}H_k(r/\epsilon,1)$ for $k = 1,2$. Then

$$\begin{aligned}\frac{\partial}{\partial\epsilon}H_k(r,\epsilon) &= (1-2k)\epsilon^{-2k}H_k(r/\epsilon,1) + \epsilon^{1-2k}(-\frac{r}{\epsilon^2})\frac{\partial}{\partial r}H_k(r/\epsilon,1)\\ &= -\frac{1}{\epsilon}((2k-1)H_k(r,\epsilon) + r\frac{\partial}{\partial r}H_k(r,\epsilon))\end{aligned}$$

The result is

$$\mathbf{u}^{fd}(\boldsymbol{x}_e) = -q_0(\hat{\boldsymbol{\beta}}\cdot\nabla)\boldsymbol{S}(\boldsymbol{x}_e - \boldsymbol{x}_0,\epsilon)\hat{\boldsymbol{\beta}} - b_0\Big(J_1(r,\epsilon)\hat{\boldsymbol{\beta}} + (\boldsymbol{x}\cdot\hat{\boldsymbol{\beta}})\boldsymbol{x}J_2(r,\epsilon)\Big)/\epsilon^2 \tag{4}$$

where $b_0 = Cq_0\epsilon$ and

$$J_1(r,\epsilon) = r\frac{\partial H_1(r,\epsilon)}{\partial r} + H_1(r,\epsilon) \tag{5}$$

$$J_2(r,\epsilon) = r\frac{\partial H_2(r,\epsilon)}{\partial r} + 3H_2(r,\epsilon) \tag{6}$$

We make the following observations about the model:

1. The regularization function that has been used extensively with the method of regularized Stokeslets is:

   $$\psi_\epsilon(r) = \frac{15\epsilon^4}{8\pi(r^2+\epsilon^2)^{7/2}}.$$

   There are many choices of regularizing functions. In order for the reduced model to have flexibility to adjust some details of its near-field velocity to match with the velocity computed by the detailed model, we choose to use a regularizing function with two undetermined coefficients that can be found as part of an optimization procedure. We use:

   $$\phi_\epsilon(r) = \frac{15a_1\epsilon^8 + 15b_1\epsilon^6r^2 + 3(42 - 8a_1 - 4b_1)\epsilon^4r^4}{16\pi(r^2+\epsilon^2)^{11/2}} \tag{7}$$

   where the coefficients guarantee that the integral of ϕ_ϵ is 1. The parameters a_1 and b_1 are to be determined based on desired flow properties. Note that this regularizing function has the same decay rate as the standard regularization function ψ_ϵ for large values of r. With the blob function in Eq. (7), we have

   $$\begin{aligned}J_1(r) = \frac{1}{1680\pi(r^2+\epsilon^2)^{9/2}}\Big(&10(-49+8a_1+3b_1)r^6\epsilon^2\\ &- 9(-196+44a_1+27b_1)r^4\epsilon^4 -\\ &9(-112+33a_1-6b_1)r^2\epsilon^6 + 2(112+37a_1+6b_1)\epsilon^8\Big)\end{aligned}$$

   and

   $$J_2(r) = \frac{1}{112\pi(r^2+\epsilon^2)^{9/2}}\Big(-2(-49+8a_1+3b_1)r^4\epsilon^2 + 3(4a_1+5b_1)r^2\epsilon^4 + 21a_1\epsilon^6\Big).$$

2. We will refer to Eq. (4) as the force-dipole model in this work. The expression for $\mathbf{u}^{fd}(\boldsymbol{x}_e)$ consists of two terms centered at the same point $\boldsymbol{x}_0$, which is assumed to represent a point along the flagellum. The first term is a regularized stresslet with coefficient q_0 that has units of force-length. The parameter q_0 in our minimal model, when divided by the regularization length ϵ, can be considered as the force generated by a flagellum. The second term is a regularized potential dipole with coefficient b_0 that has units of force-length^2. Both terms affect the flow generated by the force-dipole model of the choanoflagellate, but the values of the coefficients q_0 and b_0 may be set independently. Note that in its derivation, the value C denotes the fore-aft asymmetry of the model (Fig. 3). Since we define $b_0 = Cq_0\epsilon$, the ratio b_0/q_0 indicates a particular amount of asymmetry, which will be explored in Section 3.5. The calibration of these parameters is discussed in the next section.

2.2.3. Calibration with the detailed hydrodynamic model

Thus far, the reduced swimmer model described above depends upon the choice of the parameters a_1, b_1, ϵ in the regularization function (Eq. (7)), and the force dipole parameters b_0 and q_0 (Eq. (4)). In addition, to align the far-field flow produced by the reduced model with that produced by the detailed morphological model (e.g. Fig. 2),

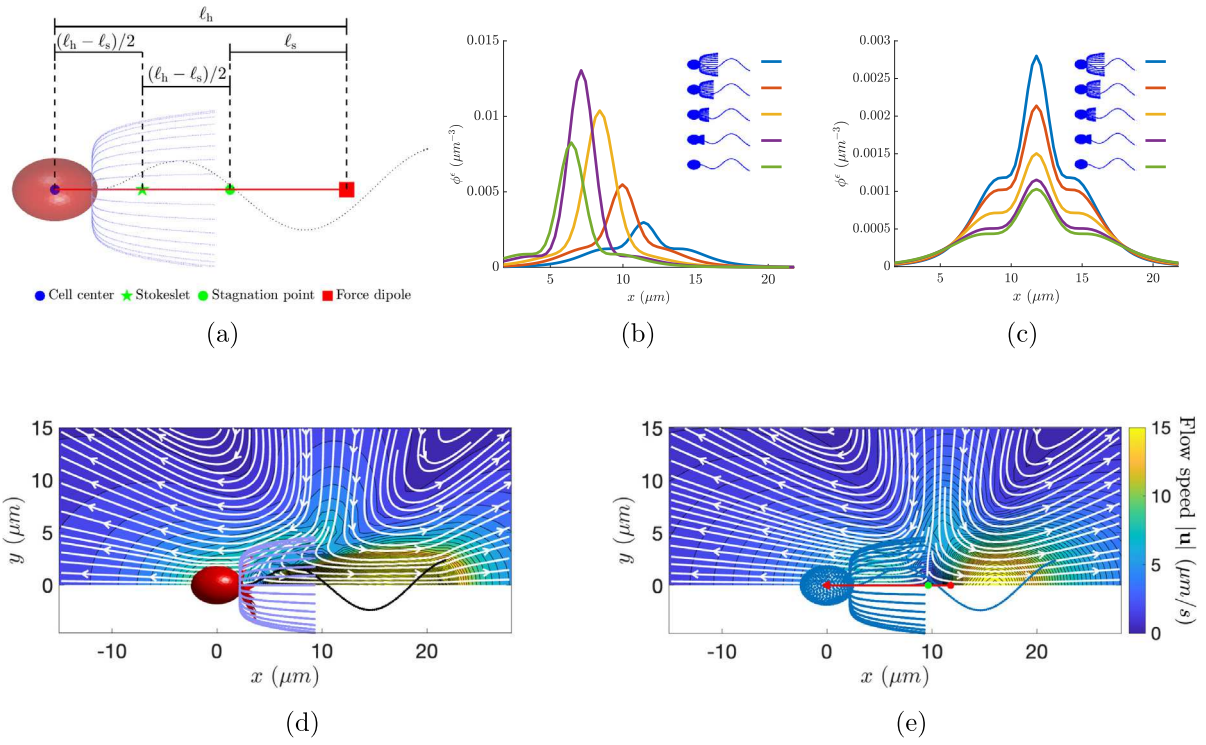

Fig. 4. Calibration of reduced model with detailed model: (a) Schematic of force dipole model showing the location of the regularized force dipole (red square) with respect to the cell body center (blue dot), the resulting stagnation point (green dot), and the location of Stokeslet forces (green star). (b) Optimized blob functions for cells with different collar lengths resulting from matching flows generated by reduced cell model with flows generated by the corresponding detailed model. We observe that the force dipole moves further from the cell center (at $x = 0$) as the collar grows. (c) Optimized blob functions when fixing the regularized force dipole at $x = 11.8$ μm. Note that peak values of the optimized blob increase with collar length. (d) Flow velocities produced by the detailed model averaged over a beating cycle and over twelve equally-spaced half-planes containing the x-axis. Parameters used in detailed model are shown in Table 1. (e) Flow velocities produced by the optimized force dipole with $q_0 = 15.7\,\text{pN}\ \mu\text{m}$, $b_0 = 9.5\,\text{pN}\ \mu\text{m}^2$, $\epsilon = 3.7$ μm, $a_1 = 0.5$, $b_1 = -1.1$, $\ell_h = 11.8$ μm.

we will also determine the position of the regularized singularities with respect to the cell center along the swimming direction $\hat{\boldsymbol{\beta}}$. The schematic in Fig. 4(a) shows this offset parameter ℓ_h. This parameter, along with the three regularization parameters and two force dipole parameters, will be chosen to best match the velocity field generated by the reduced model to that of the detailed model. Note that once this offset parameter ℓ_h is determined, the distance between the force dipole and the stagnation point, ℓ_s, along the direction $\hat{\boldsymbol{\beta}}$ is determined by solving for ℓ_s so that $\mathbf{u}^{fd}(\ell_s\hat{\boldsymbol{\beta}}) = \mathbf{0}$ (Eq. (4)). In Section 2.2.4, we will assemble the optimized force dipole cell models into colonies and place Stokeslets on the midpoints (denoted by a green star in Fig. 4(a)) between the cell center and the stagnation point of each cell to enforce the constraint that colonies move as rigid bodies. The colony velocity will be evaluated at the midpoints and we will also choose this midpoint as the point where we will evaluate a single cell's velocity.

Our procedure to find optimal reduced model parameters is as follows. To get a benchmark far-field velocity, we run the detailed morphological model of the *C. flexa* swimmer for one flagellar beat period. We evaluate the fluid velocity field at a set of discrete grid nodes around the swimmer, and average these velocities over a beat period. For the cell body centered at $[0, 0]$ μm, in the plane of flagellar beating $z = 0$ shown in Fig. 2, this region is the rectangular box $[-15, 28]\mu\text{m}\times[0, 15]\mu\text{m}$ excluding the near-field box $[2.5, 10]\mu\text{m}\times[0, 5]\mu\text{m}$. We rotate this half-planar region about the x-axis, choosing twelve half-planes at equally spaced angles around the axis, using a mesh size of 1 μm. For the reduced model, with any choice of the six parameters $(\ell_h, b_0, q_0, a_1, b_1, \epsilon)$, we can quickly evaluate the velocity field induced by this regularized singularity at the same discrete set of grid nodes using Eq. (4). Then, with respect to these six parameters, we minimize the weighted l^2 norm of the difference between the benchmark velocity field and that of the reduced model. In order to emphasize agreement in the far-field, we use the weight $y^2 + z^2$.

Fig. 4(d) shows the streamlines and velocity magnitudes, averaged over a beat period, around the detailed choanoflagellate model and Fig. 4(e) shows the streamlines due to the placement of the optimal regularized force dipole. As expected, the flow fields near and inside the microvilli collar are quite different, but the flow fields a few microns away from the organism agree nicely. We remark that in Fig. 4(e), the flow is produced by regularized elements at a single point. Figs. 4(d) and 4(e), show the calibration of the reduced swimmer with the typical *C. flexa* collar morphology and flagellar beat. We also investigate how the optimal singularity placement and regularization parameters depend upon collar size. The detailed model results shown in Fig. 2 show that the collar has an effect on where the separatrix lies in the far-field. Fig. 4(b) shows the optimal regularized functions in Eq. (7) for five model choanoflagellates, each with the same flagellar wave, but different collar lengths, from no collar up to the typical *C. flexa* collar length. The distance between the force dipole location and the cell center, ℓ_h, does indeed increase as the collar length increases (the cell body center is at $x = 0$). In order to isolate how the optimal blob function changes with collar length, we fix ℓ_h at the optimal value found for the largest collar, but otherwise solve for the other optimal parameters. In particular, panel Fig. 4(c) shows the optimal blob functions ϕ_ϵ for different collar lengths.

In [30], resistive force theory was used to estimate the force magnitude exerted by a single *C. flexa* flagellum as 6.9 pN. In order to estimate the force magnitude exerted by our reduced model of a single cell, we go back to its derivation prior to taking the limit as $\ell \to 0$ (Fig. 3). We choose ℓ to be the length scale of the cell given by the regularization parameter ϵ. This gives an estimated flagellar force magnitude of $q_0\epsilon^{-1}$. For the optimal values of ϵ and q_0 computed as

above, we find that this model force magnitude is approximately 4 pN. Additionally, we also note that flow velocities induced by the force-dipole cell model scale linearly with the parameter q_0 when the ratio b_0/q_0 is held constant.

2.2.4. A reduced colony model

We will now assemble the optimized force dipole cell models into colonies. In this work, we make the assumption that cells in colonies are rigidly held together by regularized Stokeslet forces. As such, given the flow field generated by each individual force dipole and Stokeslet force, the colony will translate and rotate as a rigid body. In order to achieve this, we will solve simultaneously for regularized Stokeslet forces at each cell location and the rigid body velocities, to satisfy free-swimming of the colony (total forces and torques generated by the colony should be zero). The location of these forces will be at the midpoint between the virtual cell center and the stagnation point.

In building a colony, we specify the position of the cell centers and the cell directions. Using the calibrated force dipole parameters, below we write down the equations that require the flow generated by the regularized force dipoles and the regularized Stokeslets to give velocities of a rigid body at the location of the Stokeslets. Denote the cell centers as $\{\boldsymbol{x}_i^{cc}, i = 1, 2, \dots, N\}$ and cell directions as $\{\hat{\boldsymbol{\beta}}_i, i = 1, 2, \dots, N\}$. Define the location of the Stokeslets by $\boldsymbol{x}_i^{mi} = \boldsymbol{x}_i^{cc} - \frac{\ell_h - \ell_s}{2}\hat{\boldsymbol{\beta}}_i$ for $i = 1, 2, \dots, N$. Based on Eq. (4), the fluid velocity at location $\boldsymbol{x}_i^{mi}$ due to a calibrated force dipole at position $\boldsymbol{x}_j$ with direction $\hat{\boldsymbol{\beta}}_j$ is

$$\begin{aligned}\boldsymbol{u}^{fd}(\boldsymbol{x}_i^{mi}) = \sum_{j=1}^{N} &-q_0(\hat{\boldsymbol{\beta}}_j \cdot \nabla)\boldsymbol{S}(\boldsymbol{x}_i^{mi} - \boldsymbol{x}_j, \epsilon)\hat{\boldsymbol{\beta}}_j \\ &- b_0\Big(J_1(r,\epsilon)\hat{\boldsymbol{\beta}}_j + ((\boldsymbol{x}_i^{mi} - \boldsymbol{x}_j)\cdot\hat{\boldsymbol{\beta}}_j)(\boldsymbol{x}_i^{mi} - \boldsymbol{x}_j)J_2(r,\epsilon)\Big).\end{aligned} \tag{8}$$

Now we can write the fluid velocities at $\boldsymbol{x}_i^{mi}$ due to the force dipoles and the Stokeslets as

$$\boldsymbol{u}^{fd}(\boldsymbol{x}_i^{mi}) + \sum_{j=1}^{N} \boldsymbol{S}(\boldsymbol{x}_i^{mi} - \boldsymbol{x}_j^{mi}, \epsilon)\boldsymbol{f}_j = \boldsymbol{U} + \boldsymbol{\Omega} \times (\boldsymbol{x}_i^{mi} - \boldsymbol{x}_0). \tag{9}$$

Here $\boldsymbol{f}_i$ is the unknown Stokeslet force and $(\boldsymbol{S}(\boldsymbol{x}_i^{mi} - \boldsymbol{x}_j^{mi}, \epsilon)\boldsymbol{f}_j)$ denotes the regularized Stokeslet flow at $\boldsymbol{x}_i^{mi}$ due to a regularized force $\boldsymbol{f}_j$ at $\boldsymbol{x}_j^{mi}$. Entries of $\boldsymbol{S}(\cdot,\cdot)$ are defined in Eq. (3). The right hand side of Eq. (9) is the velocity at $\boldsymbol{x}_i^{mi}$ of a rigid body translated with velocity $\boldsymbol{U}$ and rotated with respect to $\boldsymbol{x}_0$ with angular velocity $\boldsymbol{\Omega}$. We enforce zero total force and torque conditions

$$\sum_{j=1}^{N} \boldsymbol{f}_j = \boldsymbol{0}, \quad \sum_{j=1}^{N} \boldsymbol{f}_j \times (\boldsymbol{x}_j^{mi} - \boldsymbol{x}_0) = \boldsymbol{0} \tag{10}$$

to close the system. In this work, we choose $\boldsymbol{x}_0$ to be the origin for simplicity.

In the next section we will discuss our choice of colony surface geometries and the arrangement of individual cells. Once we have built the colony, we use the parameters obtained from the calibration as described in Section 2.2.3 and solve Eqs. (9) and (10) simultaneously for forces $\boldsymbol{f}_i, i = 1, 2, \dots, N$ and the colony translational velocity $\boldsymbol{U}$ and rotational velocity $\boldsymbol{\Omega}$. The flow velocity at any point $\boldsymbol{x}$ can then be reconstructed by

$$\boldsymbol{u}(\boldsymbol{x}) = \boldsymbol{u}^{fd}(\boldsymbol{x}) + \sum_{j=1}^{N} \boldsymbol{S}(\boldsymbol{x} - \boldsymbol{x}_j^{mi}, \epsilon)\boldsymbol{f}_j, \tag{11}$$

where $\boldsymbol{u}^{fd}(\boldsymbol{x})$ is defined in Eq. (8).

3. Results

3.1. Flagella-in colonies: lab and computational experiments

As a touchstone for our reduced model of flagella-in colonies, we start with video images collected as described in Section 2.1. These images are two-dimensional video frames, where individual cells in the colony appear at different resolutions, depending upon their position in the focal plane (see Fig. 5). Most flagella are not visible. We approximate the geometry of these spherical cup-shaped colonies by assuming that the cells are distributed on the surface of a sphere of a fixed radius. We assume that each image is a cross-section of the colony that, when rotated about its axis, sweeps out the surface of the colony. We approximate the colony width W and its length L, and use planar geometry to extract the radius R and the shape angle α of the spherical cap:

$$\alpha = \arccos\left(\frac{L^2 - 4W^2}{4W^2 + L^2}\right), \quad R = \frac{L}{2\sin\alpha}. \tag{12}$$

Fig. 5 shows images of two colonies with superimposed parameter approximations. We make two further simplifying assumptions (we will relax these in sections below). First, we assume that each cell direction (the axis of the equal and opposite forces in our reduced cell model as in Fig. 3), is perpendicular to the colony surface. Second, we assume that cells are distributed uniformly on the spherical cap. For a given frame, we count the number of cells per unit length along the perimeter ρ_d and square this quantity to approximate the cell density. This information is used to distribute cells with uniform density on the three-dimensional surface of the rotationally-symmetric spherical cap. In this work, we distribute points on a spherical cap approximately $\Delta s = 1/\rho_d$ apart in arclength, in both latitudinal and longitudinal directions. Consistent with [30], our algorithm yields a higher proportion of pentagonal neighborhoods in colonies with greater curvature.

The frame of the colony in Fig. 5(b) resembles a semicircle with approximate width $W \approx 27.0$ μm and approximate length $L \approx 51.2$ μm. It has an average cell density of 0.17 cells per μm along its perimeter, corresponding to a surface density of $\rho = .029$ cells per μm^2. Experiments show that it swims from left to right at a speed of 8.59 μm/s. Using particle image velocimetry (LaVision PIV software), trajectories of 1 μm-sized beads were tracked. Given the observed swimming speed, the particle trajectories relative to the colony can be plotted. These relative trajectories, moving from right to left, are shown in Fig. 6(a). The beads whose trajectories cross the yellow line are eventually captured by the colony (numbers indicate the end of the trajectories).

We test our reduced colony model by comparing its predictions to measured values for the living flagella-in *C. flexa* colony shown in Fig. 5(b). In our model, we approximate the colony by a spherical cap with a radius (R), shape angle (α), and cell density (determined from the number of cells per length in the frame shown in Fig. 5(b)) measured in the 2D image of the colony in the focal plane of the microscope in a frame of the video. Because the orientation and position of the colony in the focal plane can change as it swims, we run four different simulations of the colony based on R and α measured on different frames of the video (Table 2).

Our model calculations of swimming speed, particle trajectories, and water flux towards a colony are good matches for measured values. The translational velocity computed using our model of the colony in the video frame in Fig. 5(b) (simulation B, Table 2) in a fluid with viscosity of water is $|U| = 8.36$ μm/s, which is remarkably close to the experimental value of 8.59 μm/s. The range of colony speeds calculated in our four simulations are within 2 μm/s of our measured speed (Table 2). In experiments, we can measure 2D particle trajectories (Fig. 6(a)) and velocities (Fig. 7(a)) in a video frame when the focal plane of the microscope runs through the middle of a *C. flexa* colony, and we can compare them to calculated values for that same 2D plane bisecting our 3D simulation of the colony in that video frame. The paths of particles in our videos (Fig. 6(a)) are very similar to those calculated by our model (Fig. 6(b)). PIV measurements of water velocity vectors relative to a *C. flexa* colony in a focal plane bisecting the colony (Fig. 7(a)) are used to determine the radial flow velocities towards or away from the colony across a circular perimeter (radius = 45 μm). This circle

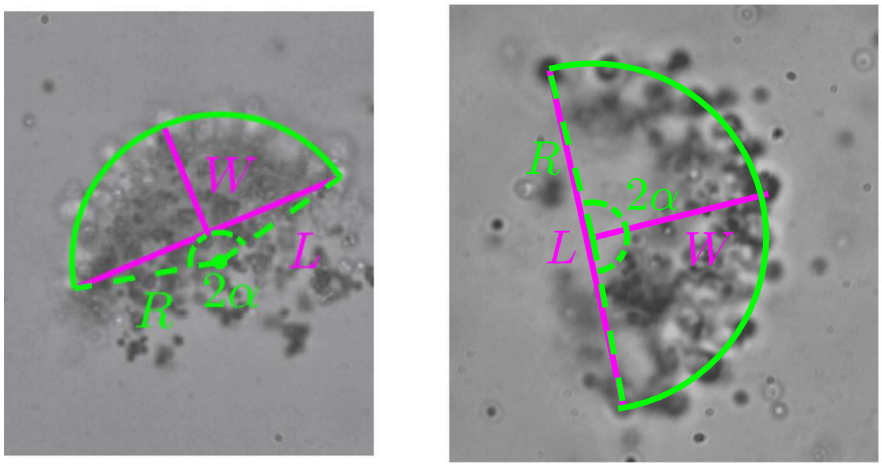

(a) W=23.6 μm, L=52.5 μm (b) W=27.0 μm, L=51.2 μm

Fig. 5. Video frames of two different flagella-in colonies. The colony width W and length L are approximated, and the spherical cap radius R and shape angle α are determined from those approximate values.

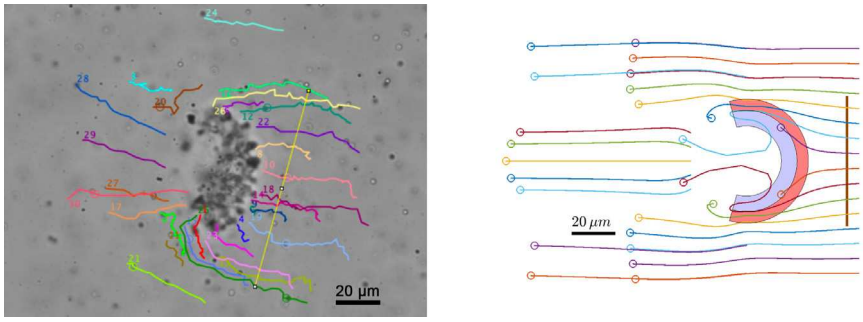

(a) (b)

Fig. 6. Particle trajectories relative to the *C. flexa* colony shown in Fig. 5(b). (a) Trajectories of beads measured in a focal plane through the middle of the living *C. flexa* colony. The beads whose trajectories cross the yellow line are eventually captured by the colony. Numbers indicate the end of the trajectories. (b) Streamlines in a plane through the middle of our 3D reduced model of that colony in the video frame shown in Fig. 5(b) (radius $R = 25.6$ μm, shape angle of $\alpha = 92.9°$; see simulation B in Table 2). Streamlines correspond to particle trajectories in this steady flow. The shaded regions indicate positions of the virtual cell bodies (red) and collars (purple).

Table 2
Model parameters and computed swimming speeds for different frames of a video of one colony (depicted in Fig. 5(b)). Colony length and width are measured in each video frame to the nearest pixel and are converted to μm's (measurement of 100 μm on a frame of a video of a stage micrometer gives a calibration factor of 288 pixels/100 μm). Colony angle and radius were calculated using Eq. (12). The measured swimming speed of the colony is 8.59 μm/s. Our model predicts similar swimming speeds for all the video frames, despite variations in colony dimensions.

	Measurements		Simulation			
	Colony width W(μm)	Colony length L(μm)	Colony radius R(μm)	Shape angle α	# of cells N	Colony speed $\|U\|$ (μm/s)
Sim. A	31.0	53.8	27.2	98.1°	155	8.10
Sim. B	26.9	51.2	25.6	92.9°	125	8.36
Sim. C	25.9	51.7	25.9	90.0°	109	7.11
Sim. D	24.1	54.4	27.4	83.0°	111	6.55
Mean	27.0	52.8	26.5	91°	125	7.53
SD/Mean	0.11	0.03	0.03	0.07	0.17	0.11

is approximately 15 μm away from the colony surface to assure that we measure steady flux towards the colony, free of artifacts due to PIV masking. Note that the total flux into the circle is not zero because fluid can enter above and below the focal plane. Using our 3D reduced model of the same colony in the same frame (Fig. 7(b)), we determine the flux through the same circular perimeter around the colony. For all of our simulations, our calculated values are a good match with the measured values (Fig. 7(c)).

Swimming velocity, bead trajectories, and flux towards the colony will surely vary with cell distributions, irregular geometries and some details of flagellar dynamics. However, the above comparison gives us confidence that this reduced colony model captures the fundamental fluid dynamics of a flagella-in, spherical cup-shaped colony. In the next section, keeping with spherical cap geometries, we will explore how variations in colony shape angles and cell densities influence the hydrodynamic performance.

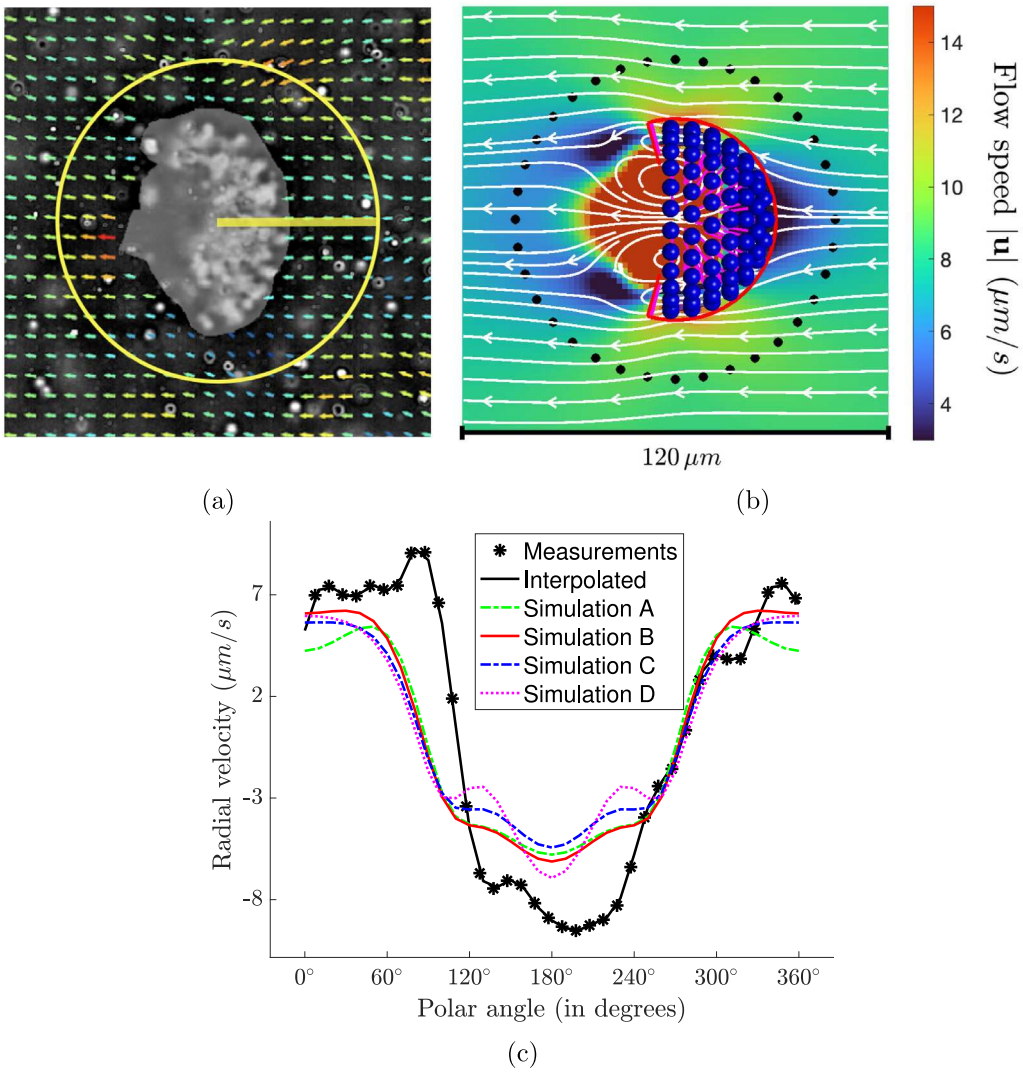

Fig. 7. Flux of water towards the *C. flexa* colony shown in Fig. 5(b). (a) PIV measurements of the water velocity vectors relative to a colony in a focal plane through the middle of the colony. Water flux in the radial direction at discrete positions across the yellow circle (radius = 45 μm) was determined from the PIV data. (b) Flow in the same plane relative to a 3D model of the same colony in the video frame shown in Fig. 5(b) (radius $R = 25.6$ μm, shape angle of $\alpha = 92.90°$; see simulation B in Table 2). White lines show streamlines relative to the colony in this plane. Water flux in the radial direction across the circle (radius = 45 μm) indicated by black dots was calculated to compare with measured values. The red line shows the intake zone of the colony itself in this plane (the region from which particles are captured by the cells in the colony; see yellow line in Fig. 6(a)). The total 3D colony intake flux across this intake zone was computed by our 3D model and results are shown in figs. 9–13. In (a,b), color scale indicates water velocity. (c) Inward normal flux at discrete positions around the circles shown in (a) and (b). The black curve indicates experimental measurements, and the other four curves show the results of simulations using colony dimensions measured in different frames of the video, as the colony changed its orientation and position relative to the focal plane. Positive values indicate flow into the circle towards the colony, and negative values indicate outward flux away from the colony.

3.2. Swimming and feeding of flagella-in, cup-shaped colonies

In this section we again consider colonies of an idealized spherical cap geometry, and we use a fixed force-dipole model of each individual cell in the colony to probe how hydrodynamic performance depends upon cell density and cap geometry. In particular, we measure both translational swimming velocity and fluid flux into an intake zone. We first start with flagella-in configurations, but then flip the direction of the virtual flagella to point outside the colonies while keeping all other model features fixed in the next section.

Our experimental observations of flagella-in colonies with shapes similar to a spherical cap spanned a range of sizes, with lengths varying from 52.5 to 78.1 μm and widths from 23.6 to 36.2 μm. The approximated shape angle values (α) ranged from 79.1° to 90.7°. When approximating these colonies by a spherical cap, these parameters give rise to a radii range from about 29 to 40 μm. The average number of cells measured along the perimeter of the cross-section of these colonies ranged from 0.16 to 0.19 cells per μm, corresponding to a surface density of $\rho = .026$ to .04 cells per μm^2. As such, we perform parameter studies of spherical cap colonies with cells distributed on spheres of radius $R = 30$ μm and $R = 40$ μm, sweeping through biologically relevant cell densities and shape angles.

As an illustration, the first row of Fig. 8 shows snapshots of spherical cup-shaped colonies, each with a shape angle of $\alpha = 90°$, but increasing surface density from left to right. The second row of Fig. 8 depicts three colonies, each with the same surface density of $\rho = .0324$ cells per μm^2, but with increasing shape angles from left to right. Also depicted are the streamlines relative to the colony, and the color intensity indicates

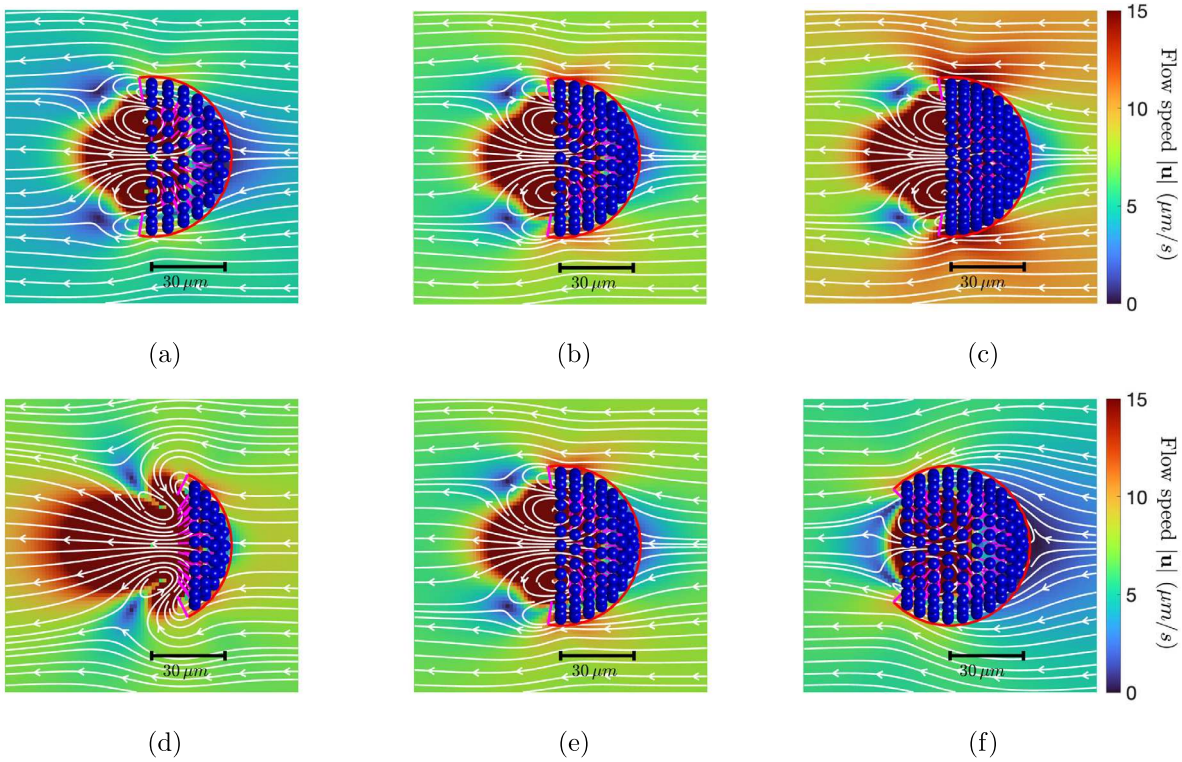

Fig. 8. Streamlines and flow magnitude, relative to the colony, for different cap geometries and different cell densities. In each snapshot, the sphere radius $R = 30$ μm. (a) $\alpha = 90°$, $\rho = .0225$ cells per μm^2. (b) $\alpha = 90°$, $\rho = .0324$ cells per μm^2. (c) $\alpha = 90°$, $\rho = .0441$ cells per μm^2. (d) $\alpha = 54°$, $\rho = .0324$ cells per μm^2. (e) $\alpha = 90°$, $\rho = .0324$ cells per μm^2 (same panel as (c)). (f) $\alpha = 126°$, $\rho = .0324$ cells per μm^2. All of these flagella-in colonies swim to the right in the lab frame, and, therefore the streamlines relative to the colony are pointing towards the left. As cell density increases, the flow velocity strengthens, leading to a higher feeding flux. The non-monotonic trend when the colony surface expands is due to two competing factors: the intake zone area increases, while the flow magnitude decreases in most areas of the intake zone.

the magnitude of the fluid velocity relative to the colony. All of these flagella-in colonies swim to the right in the lab frame, and, therefore the streamlines relative to the colony point towards the left. We observe, in the first row, that when geometry is fixed, increasing cell density increases the magnitude of the relative velocity. We observe, in the second row, that the circulation of flow into the back of the spherical cup-shaped region is more pronounced for the most shallow colony ($\alpha = 54°$), and negligible for the colony that is nearest to a closed sphere ($\alpha = 126°$). This circulation of flow can enhance fluid flux into the colony, which is important for feeding. We will quantify these observations below.

Fig. 9, panels (a) and (c), show computed translational velocities $|\mathbf{U}|$ of spherical cup-shaped, flagella-in colonies, for nine different shape angles, each at four different densities, with colonies arranged on spheres of two different radii — representing results from seventy-two simulations. (Note that while we wish to perform simulations that vary shape angle while keeping cell density fixed, there will be small variations in the chosen density due to the discrete nature of cell placement.) We remark that in the case of $R = 40$ μm, $\rho = .0625$ cells per μm^2, $\alpha = 180°$ (largest sphere, highest density, fully-closed), the number of cells exceed 1200. After placing a discrete set of cells on the spherical surfaces, simulated colonies are almost axially symmetric with respect to the horizontal axis. As all cell directions are normal to the spherical surface, the computed translational velocity is almost entirely along the horizontal axis and the computed rotational velocity is zero. In panel (a), we plot the seventy-two computed values of colony speed as a function of surface cell density. Along each curve in this panel, the same colony shape is maintained. We see that colony speed increases linearly with density — the more cells that are pushing the colony, the faster it swims. To illustrate the dependence of swimming speed on colony shape, in Fig. 9(c) we plot the same set of seventy-two computed values of colony speed as a function of the shape angle α. Each curve represents colonies with the same radius and cell density. We see that there is not a monotonic trend between colony speed and shape angle. There are two local maxima, one at $\alpha = 18°$ when the colony is nearly flat and another one near the hemisphere value $\alpha = 90°$ and 108°. There are two factors that contribute to the colony speed: the drag and the total propulsion force. As the shape angle α increases, the colony grows larger by adding more cells. For very shallow colonies, the increased drag from this colony growth outweighs the increased propulsion force from the new recruits. At some point, before the shape angle reaches that of a hemisphere, the added propulsive forces then overcome the added drag, and we see an increase in speed. However, as the colony grows past a hemisphere, the added cells' directions become less aligned with the swimming direction, and speed decreases. In the extreme case of $\alpha = 180°$, the colony is a closed sphere and does not translate.

The waving flagella of choanoflagellate cells comprising a colony create a flow that brings bacterial prey to their food-capturing collars [45]. As in previous models of choanoflagellate feeding performance (e.g. [26,29]), here we use the flux of water through an intake zone as a proxy for the rate of bacterial prey capture. We choose this intake zone to be a surface that corresponds to the region around the colony where our experiments, as in Fig. 6(a), have shown that beads enter. This intake zone is the rotationally-symmetric surface that covers the front and the side of the colony, and its one-dimensional slice is depicted in green in Fig. 1(b). The front part of the intake zone extends slightly more than a half cell length in front of the virtual cell body centers. The side part of the intake zone wraps around the regions where the virtual collars of the boundary cells would be.

For each of the seventy-two simulated flagella-in colonies, we integrate the inward normal component of the fluid velocity field (relative

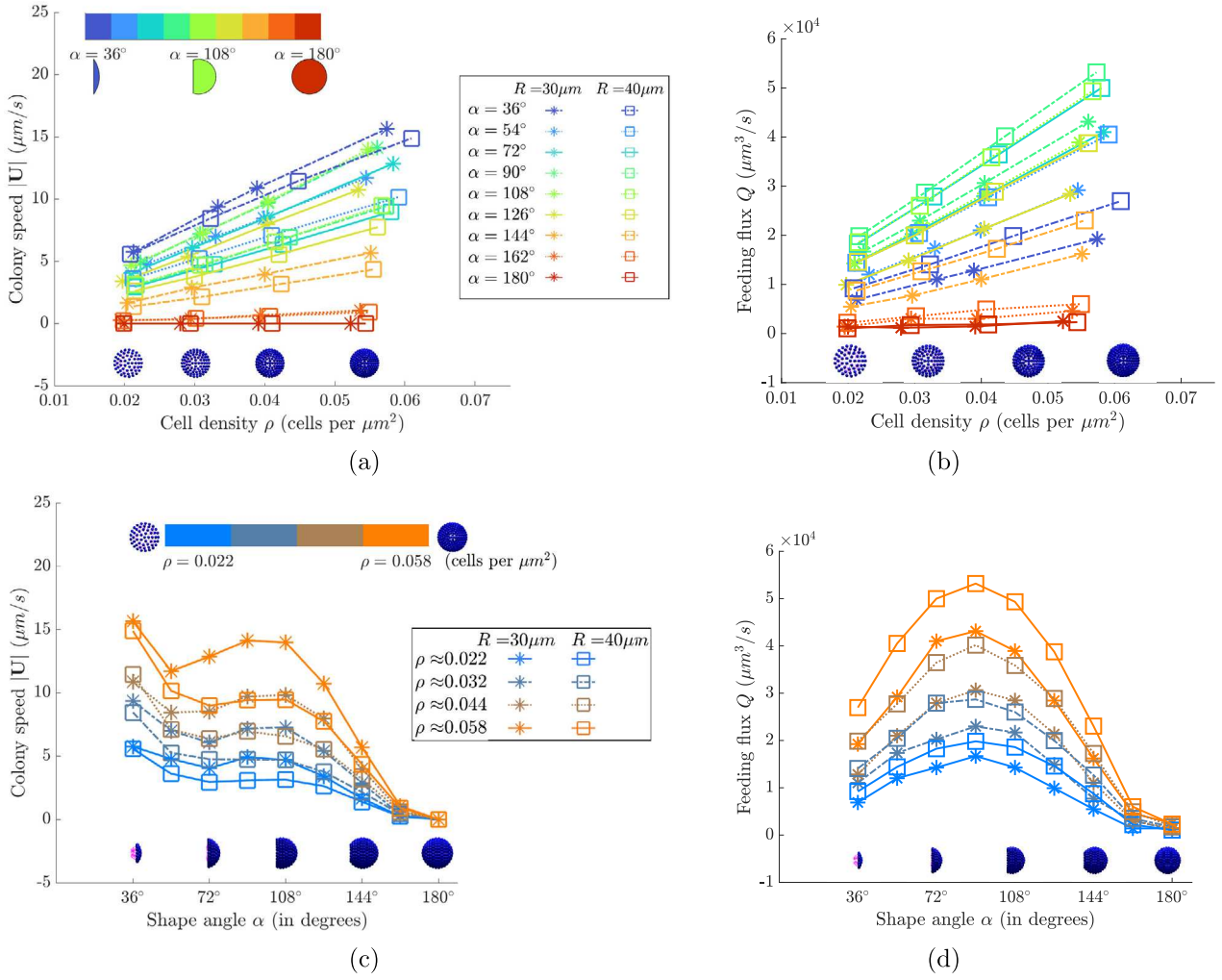

Fig. 9. Translational speeds and feeding flux of spherical cup-shaped, *flagella-in* colonies: effects of colony geometry and cell surface densities. In the lab frame, the colonies swim towards the right. (a) Colony speed and (b) feeding flux as a function of surface cell density. Each curve reflects the same colony geometry. (c) Colony speed and (d) feeding flux as a function of shape angle. Each curve reflects the same surface cell density. Note that the data points in panels (a) and (c), panels (b) and (d) are the same, just grouped differently, Swimming speed and feeding flux increase linearly in cell density but change non-monotonically as the colony surface expands from a narrow plate to a full spherical shell.

to colony translation) across the rotationally symmetric intake zone to compute the feeding flux Q, measured in $\mu m^3/s$. In Fig. 9(b), we see that for fixed colony geometries, the flux increases linearly with surface cell density. We remark that for a closed sphere, the flux is minimal, but does not vanish, as flow can enter the colony surface through the spaces between cells. In Fig. 9(d) we plot the same data points as a function of shape angle. As the shape angle α increases, the colony adds more cells and the intake zone grows, so one might expect flux to increase monotonically, but this is not the case. By looking at the flows relative to the colony in Fig. 8(d,e,f), we see that as the colony grows, its surface begins to shield the flow generated by the flagella. The shielding effect is pronounced when the shape angle is larger than $\alpha = 90°$ (the value where flux peaks).

3.3. Swimming and feeding of flagella-out, cup-shaped colonies

While hemispherical geometries are commonly observed for flagella-in *C. flexa* colonies, the flagella-out colonies are often ovoid rather than spherical cups. Nevertheless, it is instructive to use this reduced computational model to see how hydrodynamic performance changes when we flip the direction of the flagella in the simulations presented in the previous section. We keep all other model features the same except for the directions of each individual force dipole, which we change from $\hat{\boldsymbol{\beta}}$ to $-\hat{\boldsymbol{\beta}}$.

Fig. 10 shows the swimming speed and feeding flux for each of the seventy-two spherical cup-shaped colonies as in Fig. 9, but here with flagella pointing out. In the lab frame, the swimming progression of these colonies would be opposite to the flagella-in colonies. In Fig. 10(a), we see that colony speed increases linearly with surface cell density. Fig. 10(c) shows the colony speeds plotted as a function of the shape angle α. As in the flagella-in simulations, here we see that speed is not monotonic. For each density, the speed achieves a maximum between $\alpha = 54°$ and $\alpha = 72°$, which is more shallow than the hemisphere, where flagella-in colonies achieve a local maximum speed.

In order to analyze feeding flux, we choose the intake zone depicted in Fig. 1(c). Here, the front part again aligns with the virtual cell body heads (as in the flagella-in case), and the side part extends along the position of the virtual collars, which are now outside the colony. Fig.

10(b) shows the total feeding flux as a function of surface cell density. Unlike the flagella-in case, there is not a strict linear dependence on density, but beyond the lowest density values, flux increases as more cells are added to the fixed geometry. Fig. 10(d) shows the total feeding flux data re-plotted as a function of shape angle α. For each density, we see that the total feeding flux initially increases with shape angle, achieves a maximum, but then decreases as the colony approaches a closed sphere. For all but the most sparsely covered colonies ($\rho = .022$ cells μm^{-2}), the maximum value of total flux occurs for the hemisphere.

While total flux is one measure of feeding performance, we should also consider how much of this flux is achieved per cell. For all of the simulations, we present this in Fig. 11 for both flagella-in (panel (a)) and flagella-out (panel (b)) colonies as a function of shape angle α. There is an interesting collapse of data here — the flux per cell is independent of the cell density when cells are distributed on the same geometric surface. Also, as a function of shape angle α, the flux per cell decreases as the spherical cap closes, in all cases. In the flagella-in cases, colonies covering a sphere with a smaller radius show higher flux per cells than the larger radius (compare $R = 30$ μm to $R = 40$ μm). In the flagella-out case, the difference is minimal.

In summary, in this idealized geometry, when we compare the ranges of colony speed and feeding flux in Figs. 9 and 10, we do see that flagella-in colonies swim more slowly than their flagella-out counterparts, with all else being the same. In addition, we see that each flagella-in colony generates more feeding flux than the flagella-out colony.

3.4. Effects of non-uniform cell distribution on hydrodynamics

In the previous section, we assumed that cells were distributed uniformly on the surface of the colony. In this section, we investigate how swimming velocity and feeding flux is altered when cell distribution, instead, is non-uniform. To do this, we fix the shape of a flagella-in colony and fix the number of cells that comprise the colony, but vary the local cell densities as follows. We divide the colony into three regions with equal surface area as illustrated in Fig. 12(a). We label these regions on the colony surface as the *back* (purple), the *middle* (green), and the *front* (red), and prescribe cell densities by the triplet (ρ_b, ρ_m, ρ_f). The *front* region is so-designated because, given the direction that this flagella-in colony swims, it is the leading edge of the colony. These cell densities, along with the surface area of the region, determine the number of cells that will be distributed on the region. We consider flagella-in colonies of five different shapes with α ranging from 60° to 140° with $R = 25$ μm. For each of these six shapes, we consider the three cases: $(\rho_b, \rho_m, \rho_f) = (.04, .04, .04)$ cells per μm^2 (uniform case); (.02,.04,.06) cells per μm^2 (front-loaded case); and (.06,.04,.02) cells per μm^2 (back-loaded case). As in Section 3.2, we will assume that cell directions are perpendicular to the colony surface.

We will specify the cell surface densities on each region (and, hence, the number of cells), but will choose different seedings of the cells on each region. This is achieved by first distributing points on a sphere of radius R with uniform density, say ρ_f. For this distribution, we then take a random slice of the sphere that has the same shape as the front region, and use these positions as a sample of cell center locations in the front region of the non-uniform colony. This is done also for the middle and back regions. For each colony geometry, and each density triplet, we perform three hundred simulations. We remark that because the cells are not very tightly packed, the different samples may show variation in performance, as will be discussed below.

As the colony shape is rotationally symmetric about the x axis, we find that the translational velocity is mostly aligned with the x axis, with small y, z velocity components. In addition, our simulations show minimal rotational velocity, with less than 2°/s. In Fig. 12(b), we present the box plot of colony swimming velocities in the x-direction as a function of shape angle for the front-loaded, uniform, and back-loaded cases. Here each box represents the middle 50% swimming speeds across the three hundred random realizations of cell center positions on the colony surface. The medians are marked by the circular markers and the whiskers extend 1.5 times the interquartile range from the medians, and the data beyond the range defined by the whiskers, the outliers, are plotted as dots. For each shape angle, as cells are redistributed towards the back, the slower the colony swims. The front-loaded cell distributions result in faster swimming than uniform distributions, with the back-loaded cell distributions giving the worst performance. For shallow colonies, the difference is less pronounced, but as the colony fills out more of the sphere, the disparity widens. In fact, for the back-loaded case where $\alpha = 140°$, we see that the abundance of cells in the back region that push in the normal direction, actually cause the colony to reverse direction (U_x is negative). The ranges across all of the three hundred replicates are also indicated. We note that the different cell placements do not have much of an effect on colony swimming velocity.

Figs. 12(c) and 12(d) show the box plot of total feeding flux and flux per cell for each colony as a function of shape angle α for front-loaded, uniform, and back-loaded cell distributions. To show the median curves clearly, we excluded a few extreme outliers from both plots. Unlike colony velocity calculations which exhibited a small variation, we note that flux calculations have a few outliers that can be as 40 times higher. As the shape begins to exceed a hemisphere ($\alpha \approx 120°$), we see that the back-loaded colonies actually surpass the uniform colonies in feeding flux. However, for all shapes, the front-loaded colonies do the best job of bringing fluid into the intake zone of the colony. The feeding flux reported in Fig. 12(c) reports the integral over the entire intake zone of the colony. Similarly, the feeding flux per cell reported in Fig. 12(d) is computed by dividing the total flux by the total number of cells in the colony.

Now we will look more closely at the feeding flux into each of the three regions separately, as well as the flux per cell, computed separately for cells in each region. Here we focus on the single colony shape with $\alpha = 80°$, and the same density triplets as above. Again, we note that each of the three regions have the same surface areas. In Fig. 13(a), we show the medians of feeding flux into the back, middle and front region over 300 runs. We already noted that the front-loaded colonies have the highest total flux, while the back-loaded colonies have the lowest (as in Figs. 12(c) and 12(d)). In particular, Fig. 13(a) indicates that, when comparing flux into the front regions, the front-loaded colonies have roughly twice that of the uniform colonies and about five times that of the back-loaded colonies. This can be explained from the streamlines relative to the colony in Fig. 13(c,d,e). By examining the color indicating the flow speed, we see that the flow relative to the colony is significantly higher near the colony surface in the front-loaded case.

We have now observed that packing cells at the front of the colony enhances both colony swimming velocity and total flux into the colony. How, then, is the feeding of the cells that are not up front? Fig. 13(b) shows the flux per cell in each region, for the three density arrangements. We see that individual cells up in the front enjoy moderately more flux than the uniform case, and considerably more than the back-loaded case. However, what is very striking is the flux per cell for the cells in the back. There is more than a two-fold increase in feeding for these cells in the front-loaded case compared to the back-loaded case. The cells up front are helping their colony members in the back! A front-loaded cell arrangement can, therefore, promote cell division and colony growth, even for cells on the periphery.

3.5. Swimming of a complex-shaped, flagella-out colony

Our experimental data includes videos of flagella-out colonies translating and rotating as the flagella beat. These flagella-out colonies are not cup-shaped, but are typically "football-shaped", with a chunk of the football cut out. One frame of a representative movie is shown in Fig. 14(a), which depicts a cross-section of the colony. In this experimental

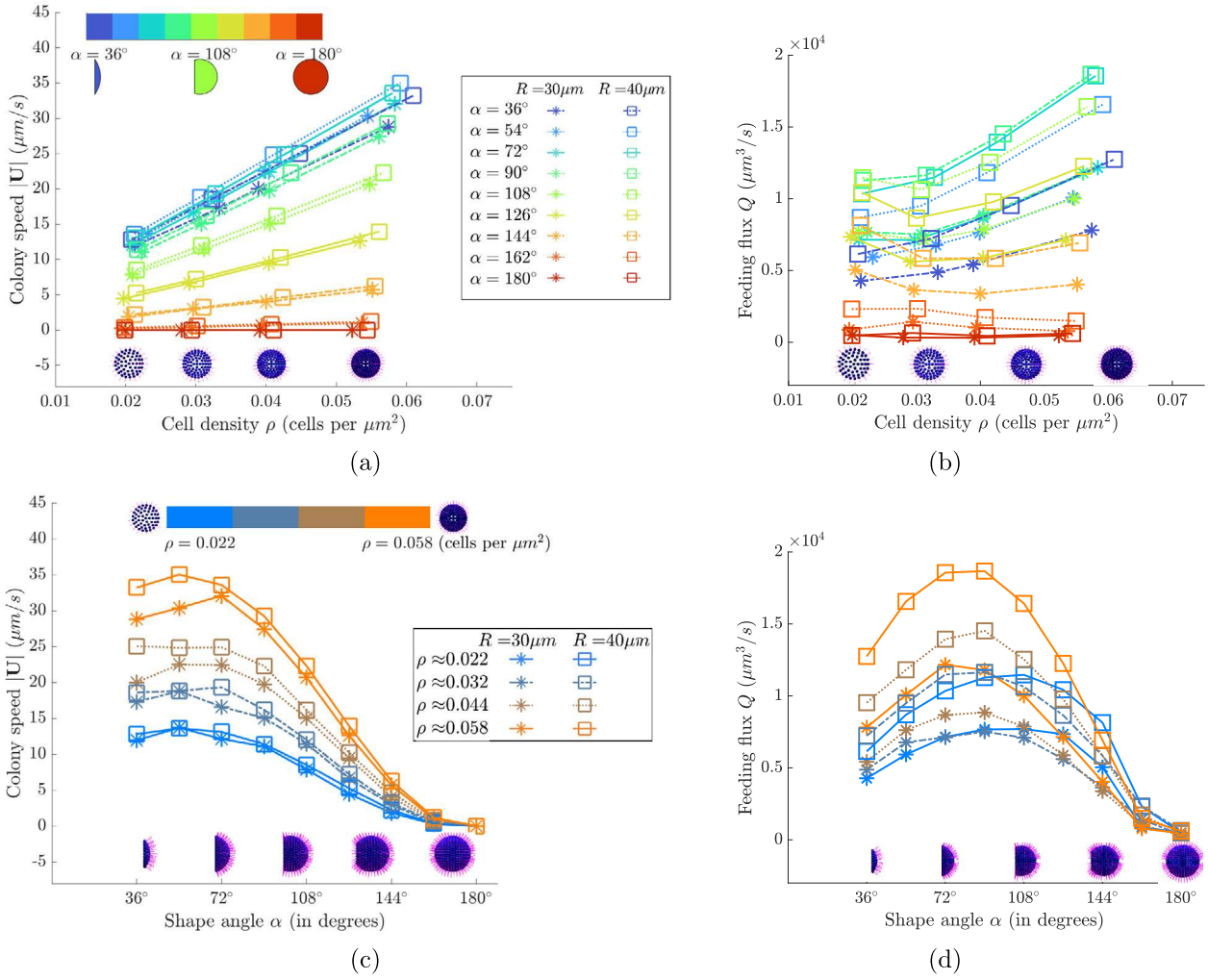

Fig. 10. Translational speeds and feeding flux of spherical cup-shaped, *flagella-out* colonies: effects of colony geometry and cell surface densities. In the lab frame, the colonies swim towards the left. (a) Colony speed and (b) feeding flux as a function of surface cell density. Each curve reflects the same colony geometry. (c) Colony speed and (d) feeding flux as a function of shape angle. Each curve reflects the same surface cell density. Note that the data points in panels (a) and (c), panels (b) and (d) are the same, just grouped differently. Similar effects of cell density and colony shape are observed. Comparing with Fig. 9, for a fixed colony shape and cell density, a flagella-out colony swims faster and has a lower feeding flux compared to its flagella-in counterpart.

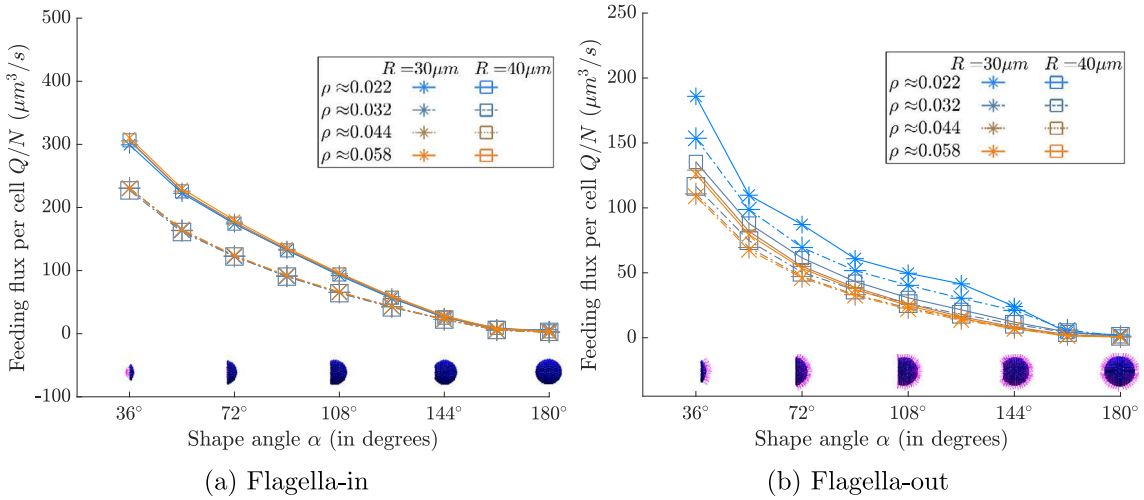

Fig. 11. Feeding flux per cell for (a) flagella-in and (b) flagella-out colonies. For each fixed colony shape and cell density, each flagella-out colony has lower flux per cell than its flagella-in counterpart.

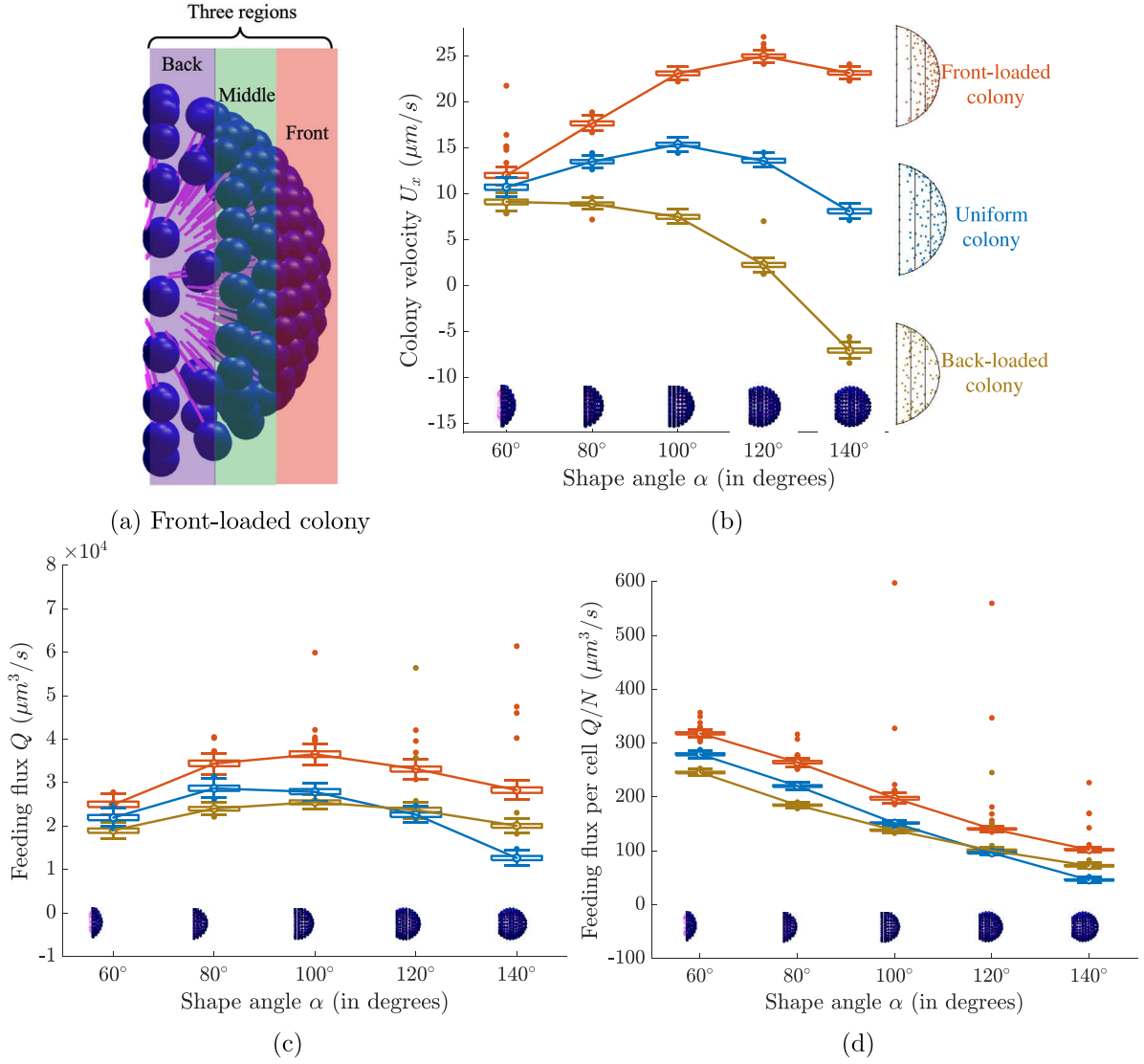

Fig. 12. (a) Schematic of a front-loaded flagella-in colony with higher density at the front. The three regions are seeded with cell surface densities (ρ_b, ρ_m, ρ_f) for back, middle and front regions respectively. (b) Box plot of colony velocities in the x-direction as a function of shape angle for spherical-cup-shaped, flagella-in colonies with $R = 25$ μm. Each box, based on 300 random cell seedings, shows the swimming speed of the central 50% of runs, with the median marked by a hollow circle. Whiskers extend 1.5 times the interquartile range from the medians, and outliers beyond this range are plotted as dots. The three curves connecting the medians correspond to colonies with cell surface densities that are either front-loaded ($\rho_b = 0.02$ cells per μm^2, $\rho_m = 0.04$ cells per μm^2, $\rho_f = 0.06$ cells per μm^2), uniform ($\rho_b = \rho_m = \rho_f = 0.04$ cells per μm^2), or back-loaded ($\rho_b = 0.06$ cells per μm^2, $\rho_m = 0.04$ cells per μm^2, $\rho_f = 0.02$ cells per μm^2). (c) Box plots of feeding flux and (d) feeding flux per cell for the same set of colonies in (a). Variations in swimming speed and flux due to random cell seeding are small, but flux can have 40 times higher outliers. Those outliers are not shown in (c,d). Front-loaded colonies swim faster than uniform colonies, with both outperforming back-loaded colonies. In terms of flux, front-loaded colonies outperform both uniform and back-loaded colonies, while back-loaded colonies surpass uniform colonies at larger shape angles.

video, the colony swims along the horizontal axis (see the black line segment in Fig. 14(a)) at 58.2 μm/s and rotates around its swimming direction at 145°/s.

Here we use the same reduced modeling approach as before, but use cell position data from the experimental images to build the computational colonies. We assume that the cells are distributed on a portion of an ellipsoidal surface rather than a sphere. Figs. 14(a) and 14(b) show two frames of the same movie at times when the colony has rotated 90°. These two frames are arranged together in the 3D image shown in Fig. 14(c). We use this geometric data to estimate the dimensions of the ellipsoidal surface (here semi-axes a, b, c are calculated to be $a = 18.1$ μm, $b = 14.6$ μm in Fig. 14(a), and $c = 14.5$ μm in Fig. 14(b)). Next we need to use the 2D images to distribute cells on the surface of the computational colony. Although not shown here, we utilize an additional experimental image where the colony has rotated 270 ° from its position in Fig. 14(a), giving us two horizontal planar images of the colony in Fig. 14(c). We project the cells from one of these two planar images to the upper half of the ellipsoidal surface, and project the cells from the other planar image to the lower half. The resulting colony model is depicted in Fig. 14(d), and we see that there is a section of the ellipsoid surface devoid of cells, reflecting the fact that the colony is not a closed surface.

Using this colony geometry with realistic cell distributions, the optimized parameters used in the previous sections for flagella-in colonies, and the assumption that the virtual flagella are perpendicular to the surface — can we predict the observed translational and rotational speeds of the colony? With these choices we find that the computational colony's swimming speed is 7.5μm/s and the rotation is at 14°/s. We see that the computational colony swims about eight times more slowly than the living colony, and rotates about ten times more slowly. We note that although both translational and rotational velocities of the colony are linear in q_0 (provided b_0/q_0 is held constant), merely scaling

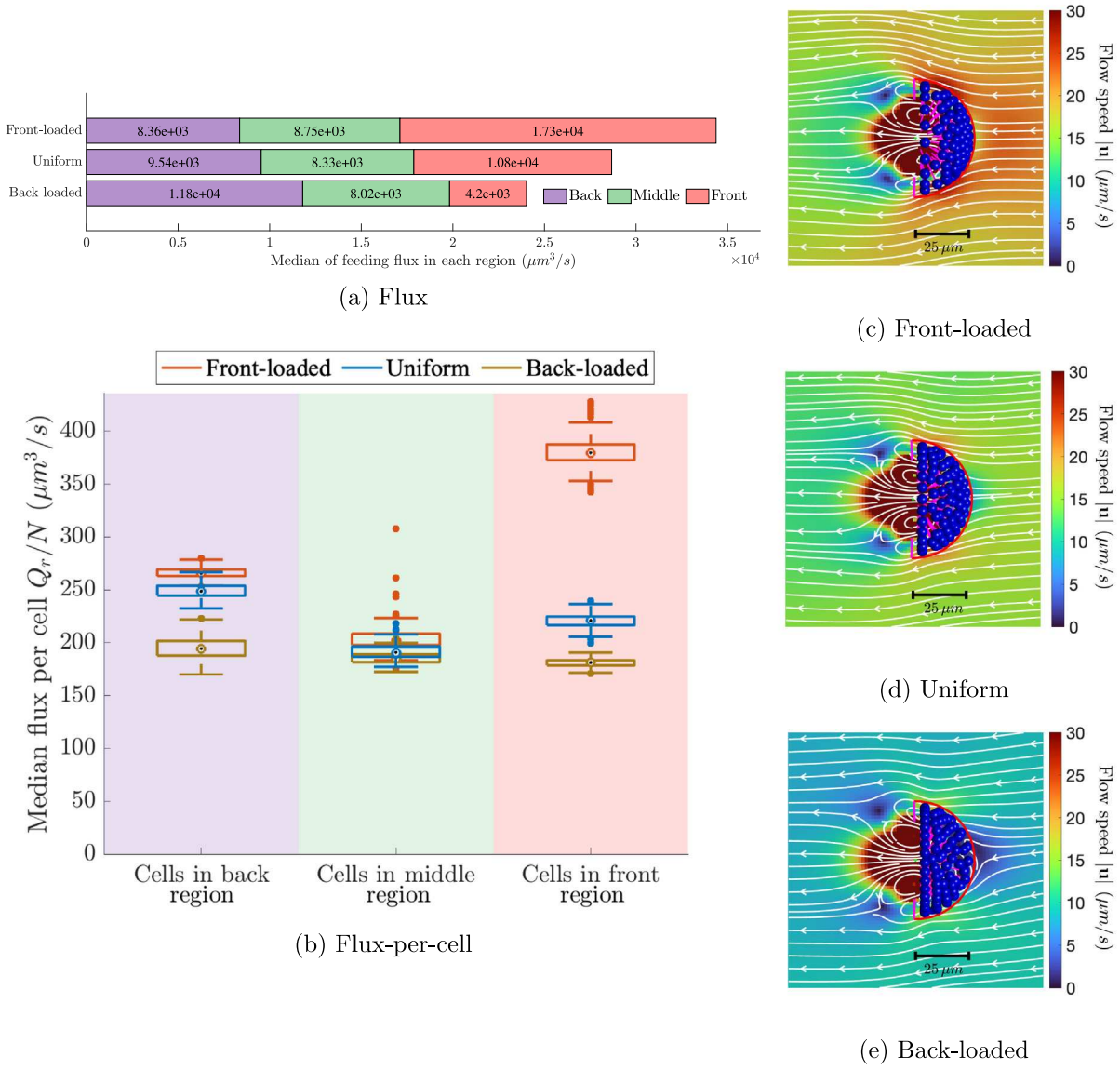

Fig. 13. (a) Median of feeding flux and (b) box plot of flux per cell in front, middle and back region as shown in Fig. 12(a). The same set of colonies of $\alpha = 80°$ in Fig. 12 is used. We show flow velocity relative to one realization of a (c) front-loaded, (d) uniform, and (e) back-loaded colony. The front-loaded colony in (c) has the highest flow speed near the intake zone.

up this swimming strength q_0 in the model to match the observed *translational* velocity will not result in a match of observed *rotational* velocity.

Perhaps the assumption that flagellar directions are always perpendicular to the surface is leading to the discrepancy between experimental and model velocities? We will first relax this assumption, and take a closer look at the experimental images. As shown in Fig. 15(a), we measure the angles made by $N_a = 27$ flagella based on one frame of the movie. The 27 angles are tabulated in the histogram shown in Fig. 15(b). Using statistics from this histogram, we perform 300 trials that vary flagellar orientation, assuming that this orientation of individual cells are independent from each other. Each trial assigns force dipole directions of each cell in the colony as follows: We randomly select an integer j between 1 and N_a, and then assign the jth tabulated angle θ_j as the angle between the force dipole direction and the vector orthogonal to the plane tangent to the colony at the cell location. Since there are infinite many directions (forming a cone) that meet the angle requirement, we select one of them from a uniform distribution.

We repeat this process 300 times and compute the linear and angular velocities for each trial. The distributions of $|\boldsymbol{U}|$ and $|\boldsymbol{\Omega}|$ are approximately Gaussian with mean 7 μm/s and 14°/s and standard deviations 1.7 μm/s and 5°/s, with maximum speeds 11 μm/s and 26°/s. This result is similar to the case of flagella perpendicular to the ellipsoid, which is not surprising since the histogram of angles indicates that the mean is near 90°. However, this procedure can also be used to investigate the effect of a bias in the flagellar orientations that favors a counter-clockwise rotation about the x-axis. After reassigning all force dipole directions with this bias and running 300 simulations, $|\boldsymbol{U}|$ and $|\boldsymbol{\Omega}|$ have means 7.9 μm/s and 60°/s, standard deviations 0.1 μm/s and 4°/s, and maximum speeds 11 μm/s and 75°/s. Similarly, reassigning all force dipole directions with a bias that favors higher swimming speed along x-axis and running 300 simulations, $|\boldsymbol{U}|$ and $|\boldsymbol{\Omega}|$ have means 16.5 μm/s and 8°/s, standard deviations 1.5 μm/s and 3°/s, and maximum speeds 21.8 μm/s and 17°/s. This shows that a bias in the flagellar orientation can significantly affect the rotation rate of the colony. However, although the rotation rate is higher, both linear

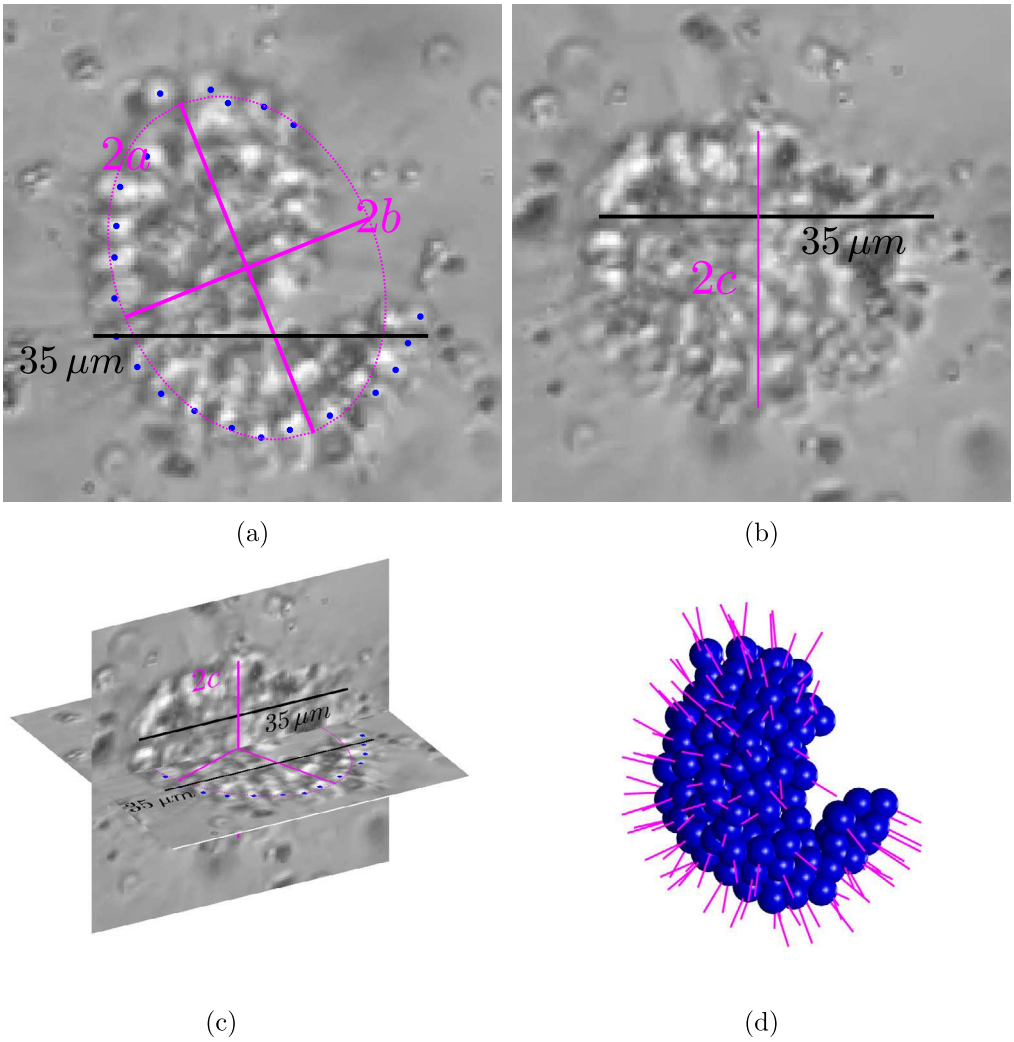

Fig. 14. Approximation of the colony as an ellipsoidal surface in (a) x–y plane and (b) along z dimension. (c) The relationship between the two selected frames in (a,b). Semi-axes a, b are measured from (a) and c is measured from (b). (d) Reconstructed colony in 3D where cell centers in (a) are mapped on or close to the ellipsoidal surface with a, b, c measured from Fig. 14. The flagellar orientations are the same as the colony in Fig. 16(b).

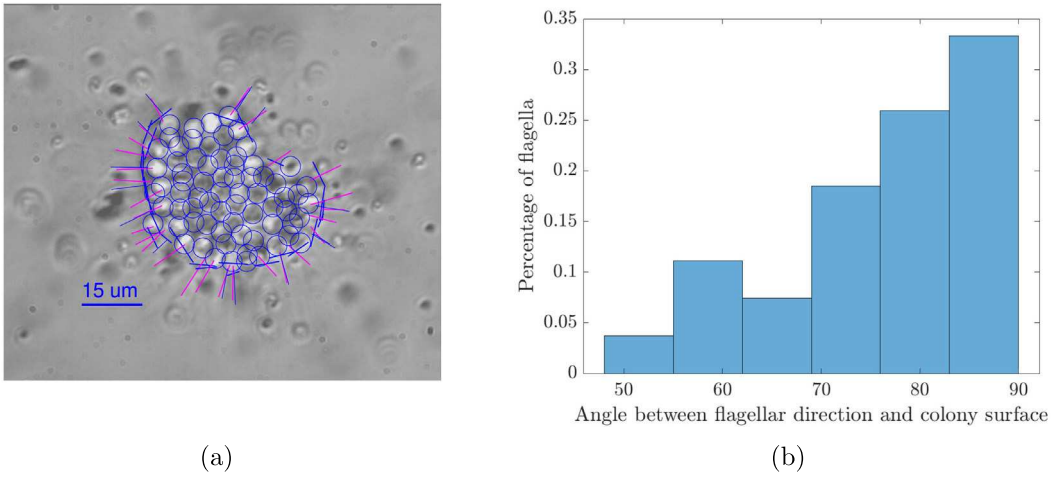

Fig. 15. (a) Measured flagellar orientations and the colony surface tangents. (b) Histogram of the flagellar angles shown as a percentage of the 27 measured. The range is $[50°, 90°]$ with 90° referring to flagellar orientations being perpendicular to the colony surface.

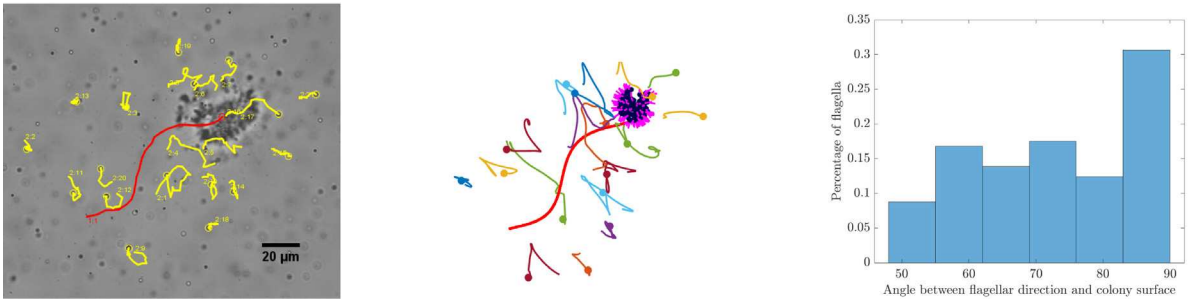

Fig. 16. (a) Colony trajectory and bead trajectories of a complex-shaped flagella-out colony in lab frame. (b) Bead trajectories relative to the flagella-out colony with a calibrated set of force dipole directions. (c) Histogram of the flagellar angles shown as a percentage of the 137 cells within the 3D colony in panel (b). The colony has $|\boldsymbol{U}| = 58.2$ μm/s and $|\boldsymbol{\Omega}| = 148°/s$. $q_0 = 126$ pN μm, $b_0 = 457$ pN μm^2, $\ell_h = 8.2$ μm. Here q_0 is 8 times bigger than that in Fig. 4(e).

and angular velocities remain well below the experimentally measured values.

While changes to the orientation of the flagella have an effect on the translational and rotational speeds of the colony, these changes cannot account for the differences between experimentally observed speeds in this flagella-out configuration. Therefore, we now hypothesize that the flagella-out beat itself must be different from the flagella-in beat. In our model, this amounts to revisiting the parameter values used in the minimal force dipole model. To test this hypothesis, we first assess the sensitivity of the resulting translational and angular velocities to the model parameters. This is done by varying q_0, b_0, and the offset ℓ_h–the three force dipole parameters that affect the far field—and use the *simulannealbnd* package of the software MATLAB to find a direction profile that matches the measured velocities. Note keeping b_0/q_0 constant corresponds to a fixed amount of front-rear asymmetry in the force dipole model, as reflected in Eq. (4). We test values of parameters $q_0, b_0/q_0$ and ℓ_h that are lower and higher than their values for the flagella-in case. The results indicate that q_0 is the most influential parameter. As discussed above, q_0 has units of force-length, and the value q_0 divided by the regularization length ϵ is interpreted as the force exerted by the flagellum of the force-dipole model. When q_0 is small, no direction profile is found to yield colony velocities close to the measured values, regardless of b_0/q_0 and ℓ_h. Once q_0 is increased by a factor of 5, a suitable direction profile is found for most values of the other parameters. At a tenfold increase in q_0, a directional profile is found for all tested combinations of b_0/q_0 and ℓ_h. These tests suggest that cells in a flagella-out colony may beat in a manner that can be modeled by a force dipole with q_0 5 to 10 times larger than the flagella-in case. As an illustration, Fig. 16(b) we show the trajectories of passive fluid markers and a colony whose 137 cells had optimized flagellar directions depicted in the histogram in Fig. 16(c). The bead trajectories in Fig. 16(a) agree qualitatively with those in Fig. 16(b), and the angle distribution in Fig. 16(c) is close to that in Fig. 15(b).

In summary, we find that increasing the flagella-in force-dipole swimming strength q_0 (force-length) by a factor of 5 to 10, and that having flagellar orientations that are not strictly perpendicular to the colony surface are needed to match the experimentally measured flagella-out translational and rotational velocities.

4. Discussion

4.1. Novel modeling approach

At the microscale, single cells with ciliated surfaces, or multicellular protozoans such as the choanoflagellate colonies discussed here, use tens to hundreds of beating cilia or flagella to swim through fluid and to produce water currents for feeding. Hydrodynamic models that capture detailed morphology and time-dependent wave kinematics of all structures would be ideal, but not feasible. The model that we present here lies within a class of models that choose a minimal depiction of flagellar force generation. These reduced models include squirmer models of ciliated cells (e.g.[46]) and rower/rotor models of beating cilia (e.g [47]). Here we develop a force-dipole model in the spirit of the previous work on choanoflagellate colonies [28,30]. In this model, we examine how the swimming and feeding performance of a *C. flexa* colony depends upon its morphology, its flagellar arrangement and flagellar forces. This reduced model is derived by a novel approach that uses the flow-field produced by a detailed computational model of a single choanoflagellate. Optimal parameters for a regularized force dipole model that best fits the flow of the detailed model are computed. This procedure selects the optimal regularized delta function from a given class. We find that this optimal function depends upon morphological features of the detailed cell model, like the presence of a color of microvilli.

We tested our reduced colony model by comparing measurements made for living *C. flexa* colonies with predictions calculated for model colonies of the same morphology. We found that the measured swimming speeds, particle trajectories, and radial flux of water produced by living flagella-in colonies match those calculated by our reduced model. For flagella-out colonies, model and measured particle trajectories also matched. However, we found that for model flagella-out colonies to swim at the same speeds that we measured for living *C. flexa* colonies, the force exerted by each flagellum of the force-dipole model (q_0 divided by the regularization length ϵ) had to be increased five to tenfold from those used for the flagella-in colonies. This suggests that flagella beat differently on flagella-out colonies than they do in flagella-in colonies.

4.2. Aspects of colony morphology that affect performance

Our modeling approach enables us to modify specific aspects of colony morphology that cannot be done experimentally with living protozoans to study the effects of each structural feature on hydrodynamic performance. To explore the selective advantages of different colony designs, we focused on aspects of performance likely to affect growth and survival: swimming (to escape predators or travel to patches of resources) and production of feeding currents. In this study, we examined how swimming and water flux of a *C. flexa* colony depends on flagellar orientation and forces, colony shape, and cell density.

Animals and choanoflagellates evolved from a common ancestor, so choanoflagellates are studied to gain insights about how the protozoan ancestors of animals might have functioned. Here we used *C. flexa* to determine the hydrodynamic consequences of having flagella covering the outer surface of a colony (as seen in many species of choanoflagellates) versus lining the inside of a cavity (a seen in sponges, primitive animals). We found that flagella-in colonies swim more slowly, but

produce higher water flux per cell than do flagella-out colonies of the same configuration (compare Figs. 9 and 10). This suggests that flagella-out colonies are better swimmers, whereas flagella-in colonies are better feeders. Indeed, both our measurements and earlier experiments by Brunet et al. showed that flagella-out colonies swam faster than flagella-in colonies, whereas flagella-in colonies captured more fluorescent beads per time [11]. In addition, these findings are consistent with those in the recent minimal hydrodynamic model of *C. flexa* in Fung et al. [30].

We used our modeling approach to determine the effect of colony shape. We discovered that flagella-in colonies shaped like bowls or hemispheres swim faster than colonies that are nearly-closed spheres, while flux is greatest towards hemispheres (Fig. 9). For flagella-out colonies, shallow bowls swim faster than other shapes, and flux to a colony is greatest for hemispheres, except at low cell densities where deep cups ($\alpha = 108°$, Fig. 10(d)) produce the greatest flux.

For each shape of colony, we examined the effects of cell density on performance. We found that for a given shape, flagella-in colonies with high cell densities swim faster and produce greater water flux towards the colony (Fig. 9), although flux per cell is independent of density (Fig. 11). For flagella-in colonies shaped like hemispherical bowls, denser packing of cells at the front of a colony increases swimming speed and raises water flux to cells at all positions in the colony (Figs. 12 and 13). Higher cell density also increases the swimming speed of flagella-out colonies (Fig. 10), but only raises flux towards the colony for shallow bowls and hemispheres. Flux per cell for flagella-out colonies is independent of cell density (Fig. 11).

Flagella-out colonies rotate as they swim. While the magnitude of the flagellar forces has the biggest effect on rotation rate, we found that the orientations of the flagella (angle between the axis of the force-dipole and the colony surface) also affect rotation rate. Colonies with all flagella perpendicular to the colony surface rotate more slowly than those with a bias in flagellar orientations. When the arrangement of cells and the distribution of flagellar angles in a model colony are similar to those of real *C. flexa* flagella-out colonies and the flagellar forces are large enough to produce measured swimming speeds, then calculated and measured rotation rates also match (Figs. 15 and 16).

4.3. Future uses of the reduced model

While our current model assumes a static colony morphology with static flagellar arrangements, its foundation is the method of regularized Stokeslets, which is a framework for capturing dynamic morphological changes of flexible, actuated structures in a viscous fluid. An intriguing aspect of *C. flexa* colonies is their ability to rapidly change their structure from flagella-in to flagella-out by active actinomyosin-mediated contraction in response to environmental signals [11,13,17–21]. Our modeling approach can be used to include the incorporation of contractile forces and flexible cell attachments in a colony to study the dynamics of this process as well as the hydrodynamic consequences.

CRediT authorship contribution statement

Hongfei Chen: Writing – review & editing, Writing – original draft, Visualization, Validation, Methodology, Investigation, Formal analysis, Conceptualization. **Tom Hata:** Writing – review & editing, Visualization, Validation, Investigation, Formal analysis, Data curation. **Ricardo Cortez:** Writing – review & editing, Writing – original draft, Validation, Methodology, Investigation, Funding acquisition, Formal analysis, Conceptualization. **Hoa Nguyen:** Writing – review & editing, Writing – original draft, Validation, Methodology, Investigation, Funding acquisition, Formal analysis, Conceptualization. **M.A.R. Koehl:** Writing – review & editing, Writing – original draft, Validation, Methodology, Investigation, Funding acquisition, Formal analysis, Data curation, Conceptualization. **Lisa Fauci:** Writing – review & editing, Writing – original draft, Validation, Methodology, Investigation, Funding acquisition, Formal analysis, Conceptualization.

Funding acknowledgment

This research was supported by NSF-DMS/NIH-NIGMS Initiative, USA to Support Research at the Interface of the Biological and Mathematical Sciences Collaborative grants 2054333 (to H.N.), 2054143 (to M.A.R.K.), 2054259 (to L.F. and R.C.), and by the Simons Foundation, USA grant SFI-MPS-SFM-00006482 to L.F.

Declaration of competing interest

The authors declare the following financial interests/personal relationships which may be considered as potential competing interests: Hongfei Chen, Tom Hata, Ricardo Cortez, Hoa Nguyen, M. A. R. Koehl, Lisa Fauci reports financial support was provided by National Science Foundation. If there are other authors, they declare that they have no known competing financial interests or personal relationships that could have appeared to influence the work reported in this paper.

Data availability

Data will be made available on request.

References

[1] F. Azam, T. Fenchel, J.G. Field, J.S. Gray, L.A. Meyer-Reil, F. Thingstad, The ecological role of water-column microbes in the sea, Mar. Ecol. Prog. Ser. 10 (1983) 257–263.
[2] S. Ohtsuka, T. Suzaki, T. Horiguchi, N. Suzuki, F. Not, Marine Protists: Diversity and Dynamics, Springer Japan, 2015.
[3] B.S.C. Leadbeater, The Choanoflagellates:Evolution, Biology and Ecology, Cambridge University Press, Cambridge, 2015.
[4] C. Fonseca, J.G. Mendonça Filho, M. Reolid, L.V. Duarte, A.D. Oliveira, J.T. Souza, C. Lézin, First putative occurrence in the fossil record of choanoflagellates, the sister group of Metazoa, Sci. Rep. 13 (2023) 1242.
[5] N. King, M.J. Westbrook, S.L. Young, A. Kuo, M. Abedin, J. Chapman, S. Fairclough, U. Hellsten, Y. Isogai, I. Letunic, M. Marr, D. Pincus, N. Putnam, A. Rokas, K.J. Wright, R. Zuzow, W. Dirks, M. Good, D. Goodstein, D. Lemons, W.Q. Li, J.B. Lyons, A. Morris, S. Nichols, D.J. Richter, A. Salamov, P. Bork, W.A. Lim, G. Manning, W.T. Miller, W. McGinnis, H. Shapiro, R. Tjian, I.V. Grigoriev, D. Rokhsar, The genome of the choanoflagellate monosiga brevicollis and the origin of metazoans, Nature 451 (2008) 783–788.
[6] D.J. Richter, N. King, The genomic and cellular foundations of animal origins, Annu. Rev. Genet. 47 (2013) 509–537.
[7] T. Brunet, N. King, The origin of animal multicellularity and cell differentiation, Dev. Cell 43 (2017) 124–140.
[8] D. Laundon, B.T. Larson, K. McDonald, N. King, P. Burkhardt, The architecture of cell differentiation in choanoflagellates and sponge choanocytes, PLoS Biol. 17 (2019) e3000226.
[9] V. Callier, Understanding the evolution of cell types to explain the roots of animal diversity, Proc. Natl. Acad. Sci. USA 117 (2020) 5547–5549.
[10] N. King, The unicellular ancestry of animal development, Dev. Cell 7 (2004) 313–325.
[11] T. Brunet, B.T. Larson, T.A. Linden, M.J.A. Vermeij, K. Mcdonald, N. King, Light-regulated collective contractility in a multicellular choanoflagellate, Science 366 (2019) 326–334.
[12] M.A.R. Koehl, Selective factors in the evolution of multicellularity in choanoflagellates, J. Exp. Zool. (2020) 1–12.
[13] N. Ros-Rocher, T. Brunet, What is it like to be a choanoflagellate? Sensation, processing and behavior in the closest unicellular relatives of animals, Anim. Cogn. 13 (2023) 1242.
[14] G.L. Mino, M.A.R. Koehl, N. King, R. Stocker, Finding patches in a heterogeneous aquatic environment: pH-taxis by the dispersal stage of choanoflagellates, Limnol. Ocean. Lett. 2 (2017) 37–46.
[15] W.E. Kumler, J. Jorge, P.M. Kim, N. Iftekhara, M.A.R. Koehl, Does formation of multicellular colonies by choanoflagellates affect their susceptibility to capture by passive protozoan predators? Eukaryot. Microbiol. (2020).
[16] N.E. Chin, T.C. Wu, J.M. O'Toole, K. Xu, T. Hata, M.A.R. Koehl, Formation of multicellular colonies by choanoflagellates increases susceptibility to capture by amoeboid predators, J. Eukaryot. Microbiol. 70 (2022) e12961.

[17] G. Jékely, Evolution: How not to become an animal, Curr. Biol. 29 (2019) R1224–R1251.
[18] J. Reyes-Rivera, Y. Wu, N.G.H. Guthrie, M.A. Marletta, N. King, T. Brunet, Nitric oxide signaling controls collective contractions in a colonial choanoflagellate, Curr. Biol. 32 (2022) 2539–2547.
[19] N.M. Nguyen, T. Merle, F. Broders-Bondon, A.C. Brunet, A. Battistella, E.B.L. Land, F. Sarron, A. Jha, J.L. Gennisson, E. Röttinger, M.E. Fernández-Sánchez, E. Farge, Mechano-biochemical marine stimulation of inversion, gastrulation, and endomesoderm specification in multicellular Eukaryota, Front. Cell Dev. Biol. 10 (2022) 992371.
[20] N. Ros-Rocher, A. Pérez-Posada, M.M. Leger, I. Ruiz-Trillo, Cell contractility in early animal evolution, Curr. Biol. 33 (2023) R966–R985.
[21] P. Tomancak, Evolutionary history of tissue bending, Science 366 (2019) 300–301.
[22] B. Orme, J. Blake, S. Otto, Modelling the motion of particles around choanoflagellates, J. Fluid Mech. 475 (2003) 333–355.
[23] B.A.A. Orme, S.R. Otto, J.R. Blake, Chaos and mixing in micro-biological fluid dynamics: blinking Stokeslets, Math. Methods Appl. Sci. 24 (2001) 1337–1349.
[24] M.E. Pettitt, B.A.A. Orme, J.R. Blake, B.S.C. Leadbeater, The hydrodynamics of filter feeding in choanoflagellates, Eur. J. Protistol. 38 (2002) 313–332.
[25] D. Smith, A boundary element regularized stokeslet method applied to cilia- and flagella- driven flow, Proc. R. Soc. A 465 (2009) 20090295.
[26] H. Nguyen, M.A.R. Koehl, C. Oakes, G. Bustamante, L. Fauci, Effects of cell morphology and attachment to a surface on the hydrodynamic performace of unicellular choanoflagellates, J. Roy. Soc. Interface 16 (2019) 20180736.
[27] L. Nielsen, S. Asadzadeh, J. Dolger, J. Walther, T. Kiorboe, A. Andersen, Cooperatively generated stresslet flows supply fresh fluid to multicellular choanoflagellate colonies, Proc. Natl Acad. Sci. USA 114 (2017) 9373–9378.
[28] M. Roper, M.J. Dayel, R.E. Pepper, M.A.R. Koehl, Cooperatively generated stresslet flows supply fresh fluid to multicellular choanoflagellate colonies, Phys. Rev. Lett. 110 (228104) (2013).
[29] J. Kirkegaard, R. Goldstein, Filter-feeding, near field flows, and the morphologies of colonial choanoflagellates, Phys. Rev. E 94 (052401) (2016).
[30] L. Fung, A. Konkol, T. Ishikawa, B.T. Larson, T. Brunet, R.E. Goldstein, Swimming, feeding, and inversion of multicellular choanoflagellate sheets, Phys. Rev. Lett. 131 (2023) 168401.
[31] Y. Ashenafi, P.R. Kramer, Statistical mobility of multicellular colonies of flagellated swimming cells, Bull. Math. Biol. 86 (2024) 125.
[32] S.E. Spagnolie, E. Lauga, Hydrodynamics of self-propulsion near a boundary: predictions and accuracy of far-field approximations, J. Fluid Mech. 700 (2012) 105–147.
[33] K. Drescher, J. Dunkel, L.H. Cisneros, S. Ganguly, R.E. Goldstein, Fluid dynamics and noise in bacterial cell-cell and cell-surface scattering, Proc. Natl. Acad. Sci. USA 108 (27) (2011) 10940–10945.
[34] K. Ishimoto, E.A. Gaffney, B.J. Walker, Regularized representation of bacterial hydrodynmaics, Phys. Rev. Lett. 5 (2020) 093101.
[35] E. Lushi, C.S. Peskin, Modeling and simulation of active suspensions containing large numbers of interacting micro-swimmers, Comput. Struct. 122 (2013) 239–248.
[36] J. Deng, M. Molaei, N.G. Chisholm, K.J. Stebe, Interfacial flow around a pusher bacterium, J. Fluid Mech. 976 (2023) A18.
[37] P.T. Underhill, J.P. Hernandez-Ortiz, M.D. Graham, Diffusion and spatial correlations in suspensions of swimming particles, Phys. Rev. Lett. 100 (2008) 248101.
[38] B. Delmotte, E.E. Keaveny, F. Plouraboué, E. Climent, Large-scale simulation of steady and time-dependent active suspensions with the force-coupling method, J. Comput. Phys. 302 (2015) 524–547.
[39] K. Ishimoto, E.A. Gaffney, Squirmer dynamics near a boundary, Phys. Rev. E 88 (6) (2013) 062702.
[40] I.O. Götze, G. Gompper, Mesoscale simulations of hydrodynamic squirmer interactions, Phys. Rev. E 82 (4) (2010) 041921.
[41] P. Boindala, New Minimal Representations of Self-Propelled Swimmers in Low Reynolds Number Regime Using Regularized Fundamental Solutions with Applications to Collective Flow (Ph.D. thesis), Tulane University, 2010.
[42] A. Hoover, P. Boindala, R. Cortez, A regularized force doublet framework for self-propelled microswimmers, J. Fluid Mech. (2024) R1.
[43] R. Cortez, L. Fauci, A. Medovikov, The method of regularized Stokeslets in three dimensions: Analysis, validation, and application to helical swimming, Phys. Rev. Lett. 17 (2005) 031504.
[44] R. Cortez, D. Varela, A general system of images for regularized Stokeslets and other elements near a plane wall, J. Comput. Phys. 285 (2015) 41–54.
[45] H. Nguyen, E. Ross, R. Cortez, L.J. Fauci, M.A.R. Koehl, Effects of prey capture on the swimming and feeding performance of choanoflagellates, Flow 3 (2023) E22.
[46] Eric Lauga, The Fluid Dynamics of Cell Motility, Cambridge University Press, 2016.
[47] Nicolas Bruot, Pietro Cicuta, Emergence of polar order and cooperativity in hydrodynamically coupled model cilia, J. Roy. Soc. Interface 10 (2013) 20130571.